Atmos. Chem. Phys., 19, 2601–2627, 2019
https://doi.org/10.5194/acp-19-2601-2019

Atmospheric Chemistry and Physics
Open Access
EGU

Aerosol effects on deep convection: the propagation of aerosol perturbations through convective cloud microphysics

Max Heikenfeld[1], **Bethan White**[1,2], **Laurent Labbouz**[1,3], **and Philip Stier**[1]

[1]Atmospheric, Oceanic and Planetary Physics, Department of Physics, University of Oxford, Oxford, UK
[2]ARC Centre of Excellence for Climate System Science, School of Earth, Atmosphere and Environment, Monash University, Melbourne, Australia
[3]Laboratoire d'Aérologie, Université de Toulouse, CNRS, UPS, Toulouse, France

Correspondence: Max Heikenfeld (max.heikenfeld@physics.ox.ac.uk)

Received: 19 June 2018 – Discussion started: 30 August 2018
Revised: 5 February 2019 – Accepted: 10 February 2019 – Published: 28 February 2019

Abstract. The impact of aerosols on ice- and mixed-phase processes in deep convective clouds remains highly uncertain, and the wide range of interacting microphysical processes is still poorly understood. To understand these processes, we analyse diagnostic output of all individual microphysical process rates for two bulk microphysics schemes in the Weather and Research Forecasting model (WRF). We investigate the response of individual processes to changes in aerosol conditions and the propagation of perturbations through the microphysics all the way to the macrophysical development of the convective clouds. We perform simulations for two different cases of idealised supercells using two double-moment bulk microphysics schemes and a bin microphysics scheme. The simulations cover a comprehensive range of values for cloud droplet number concentration (CDNC) and cloud condensation nuclei (CCN) concentration as a proxy for aerosol effects on convective clouds. We have developed a new cloud tracking algorithm to analyse the morphology and time evolution of individually tracked convective cells in the simulations and their response to the aerosol perturbations.

This analysis confirms an expected decrease in warm rain formation processes due to autoconversion and accretion for more polluted conditions. There is no evidence of a significant increase in the total amount of latent heat, as changes to the individual components of the integrated latent heating in the cloud compensate each other. The latent heating from freezing and riming processes is shifted to a higher altitude in the cloud, but there is no significant change to the integrated latent heat from freezing. Different choices in the treatment of deposition and sublimation processes between the microphysics schemes lead to strong differences including feedbacks onto condensation and evaporation. These changes in the microphysical processes explain some of the response in cloud mass and the altitude of the cloud centre of gravity. However, there remain some contrasts in the development of the bulk cloud parameters between the microphysics schemes and the two simulated cases.

1 Introduction

Deep convective clouds are an important feature of the Earth's atmosphere, ranging from widespread convection dominating the atmosphere in the tropics to mid-latitude convective systems (Emanuel, 1994). The impact of aerosols on ice- and mixed-phase processes in convective clouds remains highly uncertain (Tao et al., 2012; Varble, 2018), which has implications for determining the role of aerosol–cloud interactions in the climate system. Representing these effects in global climate models poses additional challenges due to the relatively small length scales often less than a few kilometres at which convective clouds develop and because of limitations in the representations of microphysical processes in the convective parameterisations (Tao et al., 2012; Boucher et al., 2013; Sullivan et al., 2016), with only few models explicitly representing the effects of aerosols on deep convective clouds (e.g. Song and Zhang, 2011; Guo et al., 2015; Kipling et al., 2017; Zhang et al., 2017; Labbouz et al., 2018). The highly localised nature of convective processes also leads to major

challenges in observations both from satellites and aircraft measurements (Rosenfeld et al., 2014).

Over recent years numerous studies using cloud-resolving model simulations (CRM) have investigated aerosol–convection interactions in various set-ups, ranging from case study simulations to idealised simulations of squall lines or supercells like the cases used in this study (Seifert and Beheng, 2006; Storer et al., 2010; Morrison, 2012; Kalina et al., 2014). The results, however, vary strongly between many of these studies. The differences can be attributed to the simulation of different types of convection or different environmental conditions like humidity or wind shear, but are also related to differences between the models or modelling approaches used (Tao et al., 2012; Fan et al., 2016; White et al., 2017). These challenges in modelling are strongly related to numerous interacting physical processes (Fan et al., 2016) in cloud microphysics and to the interaction between clouds and other processes in the atmosphere on different scales (Tao et al., 2012). In addition to the analysis of process rates in numerical simulations, analytical evaluations of the microphysical rate equations of the microphysics schemes can give important insights into the propagation of aerosol effects in the cloud microphysics (Glassmeier and Lohmann, 2016). This kind of analytical approach works well for warm-phase clouds but is less conclusive for the response of mixed-phase clouds, especially deep convective clouds, due to many compensating effects and the complexity of the processes involving ice-phase hydrometeors (Glassmeier and Lohmann, 2016).

Convective invigoration (Andreae et al., 2004; Rosenfeld et al., 2008; Lebo and Seinfeld, 2011) has been proposed as a mechanism by which aerosols impact the development of deep convective clouds. A higher number concentration of aerosols suitable for acting as cloud condensation nuclei (CCN) can lead to more but smaller cloud droplets, which are less likely to be processed into rain and precipitated out of the cloud. This would lead to more water reaching the freezing level in the cloud where subsequent freezing leads to additional latent heating in the higher levels of the cloud, enhancing the strength of the convection with higher updraft speeds and cloud-top height. Other studies point out the additional impact of the larger number of aerosols, and subsequently cloud droplets, leading to smaller ice particles, which then favours increased cloud fraction, cloud-top height, and cloud thickness (Fan et al., 2013) due to reduced fall speeds of the ice particles. This implies a significant radiative effect on the climate system through enhanced anvils (Koren et al., 2010). Grabowski and Morrison (2016) argue that the effects can be purely attributed to the effects of smaller droplets and ice crystals, with negligible effects of the thermodynamic enhancement proposed in Rosenfeld et al. (2008). Some of the differences in the assessments of convective invigoration due to aerosols are actually caused by the difference in the definition of both changes in aerosol and the quantification of the strength of convection based on different variables such as surface precipitation, updraft speeds or cloud-top heights (Lebo et al., 2012; Altaratz et al., 2014). Significant mechanisms buffering the impact of aerosols on clouds and precipitation, both with a focus on warm-phase processes (Stevens and Feingold, 2009) and for mixed-phase and ice clouds (Fan et al., 2016), have been proposed. However, recent studies question the attribution of observed relationships between aerosol concentrations and cloud-top height to aerosol microphysical effects (Varble, 2018; Nishant and Sherwood, 2017). It is, therefore, one of the main goals of this paper to investigate whether and how these proposed mechanisms of convective invigoration, especially the proposed invigoration of convection due to additional latent heat release from freezing, manifest themselves in numerical simulations.

Many studies have pointed out the representation of cloud microphysics in models as one of the main sources of uncertainty in high-resolution model studies of aerosol–cloud interactions or cloud feedbacks to a warming climate, especially for mixed-phase and ice-phase clouds (Tao et al., 2012; Khain et al., 2015; White et al., 2017). This also holds for the role of the microphysics schemes in global model simulations of both convection and aerosol–cloud interactions (Lohmann and Feichter, 2005; Gettelman, 2015; Malavelle et al., 2017).

Most currently used cloud microphysics schemes can be separated into two approaches, bulk microphysics schemes and bin microphysics schemes (Khain et al., 2015). Bulk microphysics schemes assume a specific size distribution for a range of different hydrometeor classes and describe their evolution and interactions based on a certain number of moments of these distributions. Double-moment schemes with both prognostic mass and number concentrations of the hydrometeors are the current standard and necessary to meaningfully represent aerosol–cloud interactions (Khain et al., 2015; Igel et al., 2014).

The separation of the hydrometeors into individual hydrometeor classes in microphysics schemes brings with it specific challenges in resolving the microphysical processes. In bulk schemes, liquid water in the cloud is separated into cloud droplets and raindrops. The collision–coalescence processes leading to the formation of rain from cloud droplets have to be parameterised through the artificial process of droplet autoconversion and a simplified treatment of accretion of droplets by raindrops. The semi-empirical nature of these parameterisations has been shown to be the source of major uncertainty in the assessment of aerosol–cloud interactions in numerical model simulations (Khain et al., 2015; White et al., 2017). In the ice phase, most current microphysics schemes separate the hydrometeors into a number of different classes such as pristine ice, snow, hail or graupel. The equations and parameters for the calculation of the microphysical process rates as well as important physical properties of the hydrometeors, such as shape, density or the specific form of the size distribution, are specified for each individual hydrometeor class. These choices additionally im-

pact important physical processes such as the fall speeds of hydrometeors in the calculation of sedimentation or the radiative properties of the hydrometeors. This can lead to abrupt changes to the evolution of the cloud due to a change in the partition between the hydrometeor classes in the ice phase of the cloud (Morrison and Milbrandt, 2014). There have been developments towards overcoming the separation of ice hydrometeors into fixed individual classes (Harrington et al., 2013a, b; Morrison and Milbrandt, 2014; Morrison et al., 2015) by treating ice-phase hydrometeors as one single class with smoothly varying physical properties, which have been implemented in both cloud-resolving models and in global climate models. Nevertheless, most current applications rely on microphysics schemes performing the separation into different hydrometeor classes. Better understanding the possible effects and causes of shifts in the hydrometeor partitions through the comprehensive analysis of the microphysical pathways in the two bulk microphysics schemes is thus a main focus of this paper.

Bin microphysics schemes represent the different hydrometeors in the cloud through a number of individual size bins per hydrometeor class, thus allowing for more flexible representation of the actual size distribution and the interaction between the different size bins (Khain et al., 2015). Due to the large number of simulated variables, however, this approach results in high computational cost. One of the main benefits is avoiding the artificial separation between cloud droplets and raindrops that causes challenges in bulk microphysics schemes, for example in the form of a parameterisation of the autoconversion processes (Khain et al., 2015). The representation of ice-phase hydrometeors in typical bin microphysics schemes, however, is based on separate hydrometeor classes as in the bulk schemes, each individually resolving their size distribution through a number of bins (Khain et al., 2015). While many studies have proposed that bin-resolving microphysics schemes are necessary to reliably represent possible microphysical aerosol effects on convective clouds (Khain et al., 2004; Fan et al., 2012, 2016) in model simulations, a large range of studies and applications, e.g. routine numerical weather prediction (NWP), coupled simulations with a complex aerosol and chemistry and global climate model simulations as well as a large number of CRM-based studies of aerosol–cloud interactions apply bulk microphysics schemes.

This study aims to unravel the underlying microphysical mechanisms responsible for the large diversity of simulated aerosol effects on convection through a comprehensive analysis of the propagation of aerosol perturbations through microphysical pathways in different microphysics schemes.

Tracking individual convective cells in the simulation makes it possible to draw direct conclusions about the behaviour of individual convective cells in the simulations, e.g. regarding their time evolution or the response to changes in simulation parameters that go beyond the bulk average over the simulation domain or the sum of all cloudy areas in the simulation. The analysis of tracked cumulus clouds has been applied in previous studies (e.g. Dawe and Austin, 2012; Heus and Seifert, 2013; Heiblum et al., 2016a, b) with a focus on various aspects of convective clouds, including the effects of aerosol perturbations on deep convection (Terwey and Rozoff, 2014).

We have implemented detailed microphysical process-rate diagnostics for pathway analysis in the two double-moment microphysics schemes of Morrison et al. (2009) and Thompson et al. (2004). We analyse the cloud morphology and the spatial structure of the microphysical processes in individual tracked convective cells. We display the microphysical process rates in the form of scaled pie charts. This has been inspired by previous studies using this type of visualisation of the spatiotemporal development of physical processes for other applications. Schutgens and Stier (2014) performed a pathway analysis for the aerosol processes in a global climate model (ECHAM-HAM). Chang et al. (2015) applied a microphysical pathway analysis including a similar visualisation of process rates to simulations of pyro-convective clouds, however, using a much simpler two-dimensional model for highly idealised individual clouds.

In addition to the detailed process-rate diagnostics, we derive important bulk cloud properties, such as the total cloud mass or the altitude of the centre of gravity, and analyse their evolution over the life cycle of the tracked cells. Our approach goes beyond previous studies with a similar set-up (Morrison et al., 2009; Kalina et al., 2014) that mainly focussed on domain average properties and only a specific subset of microphysical processes.

We use a well-documented idealised supercell set-up based on Weisman and Klemp (1982, 1984), which was applied in previous studies (e.g. Khain and Lynn, 2009; Morrison et al., 2009; Kalina et al., 2014), to create a well-defined development of a strong convective cell, allowing us to focus on the microphysical evolution of individual convective cells. To test the representativeness of our results from this first case, we include simulations for a second idealised supercell case based on the measurements and model set-ups from Kumjian et al. (2010); Naylor and Gilmore (2012); Dawson et al. (2013).

We represent idealised aerosol perturbations through changes to a fixed cloud droplet number concentration (CDNC) in each simulation with the two bulk microphysics schemes. This allows us to isolate the actual cloud microphysical pathways from uncertainties in the representation of the activation of CCN in numerical models (Ghan et al., 2011; Simpson et al., 2014; Rothenberg et al., 2018). Simulations are performed for a comprehensive range of CDNC for each microphysics scheme ranging from values representative of very clean, maritime conditions (CDNC $= 50\,\mathrm{cm}^{-3}$) to very polluted situations (CDNC $= 2500\,\mathrm{cm}^{-3}$).

We compare the results to simulations performed with a bin microphysics scheme (HUJI spectral-bin scheme) for a subset of the analyses to investigate whether the effects investigated in more detail through the microphysical pathway

analysis for the two bulk microphysics schemes agree with the response of a bin microphysics scheme to perturbations of aerosol proxies.

2 Methods

2.1 Model set-up

The simulations are performed with the Weather and Research Forecasting model (WRF) version 3.7.1 (Skamarock et al., 2008). We use the two-moment microphysics schemes from Thompson et al. (2004, 2008), denoted as THOM, and from Morrison et al. (2005, 2009), called MORR in our figures and tables. To isolate the role of cloud microphysics for aerosol effects on deep convection from additional uncertainties in model-simulated aerosol fields, we apply a fixed CDNC in the two bulk microphysics schemes for each simulation. In each of the schemes, the CDNC is reset to the chosen value at the end of each model time step in all cloudy grid points. We vary this CDNC value between different simulations as a proxy for aerosol number concentration. There are versions of both bulk microphysics schemes that include the activation of a fixed CCN spectrum or even interactive aerosols (Thompson and Eidhammer, 2014; Wang et al., 2013). However, the implementation of both the cloud droplet activation and the representation of the aerosol distributions is very different between the two microphysics schemes, which would add additional differences between the schemes compared to representing the perturbations in the form of a varying CDNC.

The detailed analyses of the process rates in this paper are carried out for simulations using the two bulk microphysics schemes. To investigate how the results obtained from the detailed analysis of the two bulk microphysics schemes hold for a bin cloud microphysics scheme, we also include additional simulations with the Hebrew University cloud model (HUCM) spectral-bin microphysics scheme (Khain et al., 2004; Lynn et al., 2005a, b), called SBM in the rest of the paper. We perform a subset of the analyses for this microphysical scheme, excluding the detailed microphysical process-rate analysis but including the analysis of changes to the hydrometeor mixing ratios and the bulk cloud properties. We use the full version of the spectral-bin microphysics scheme in WRF (Khain et al., 2012) and perform a variation of CCN number concentration.

Both bulk microphysics schemes make use of saturation adjustment, removing all water vapour exceeding the saturation vapour pressure in each time step and instantaneously condensing it to cloud water at each time step. This prevents a build-up of supersaturation in strong updrafts and can thus impact effects of perturbations in the microphysics (Lebo et al., 2012). The bin microphysics scheme (SBM) includes an explicit calculation of supersaturation in the microphysics at each time step and allows for a build-up of supersaturation in strong updrafts over several time steps.

We simulate two different idealised supercell cases. The first set of simulations (CASE1) is based on the default WRF quarter-circle shear supercell case representative of a supercell case over the southern Great Plains of the United States (Khain and Lynn, 2009; Lebo and Seinfeld, 2011). This case uses an initial sounding described in Weisman and Klemp (1982) with a surface temperature of 300 K and a surface vapour mixing ratio of $14\,\mathrm{g\,kg^{-1}}$. The wind profile is taken from Weisman and Rotunno (2000) and features a wind shear of $40\,\mathrm{m\,s^{-1}}$ made up of a quarter-circle shear up to a height of 2 km and a linear shear further up to 7 km height. The initiation of convection is triggered by a warm bubble with a magnitude of 3 K in potential temperature centred at 1.5 km height in the centre of the domain with a radius of 10 km horizontally and 1.5 km vertically in which the perturbation decays with the square of the cosine towards the edge of the bubble (Morrison, 2012). This type of set-up has been used for a number of similar studies in the past (Storer et al., 2010; Morrison and Milbrandt, 2010; Morrison, 2012; Kalina et al., 2014).

To test the representativeness of the results for different cases of idealised deep convection, a set of simulations for a second supercell case (CASE2) is based on an observed supercell storm over Oklahoma in 2008 (Kumjian et al., 2010). In contrast to the first case, the initial profiles are from observations used in the model experiments in Dawson et al. (2013). This case features a significantly drier initial profile with a surface temperature of 308 K and a surface water vapour mixing ratio of $16\,\mathrm{g\,kg^{-1}}$ along with wind shear of similar magnitude to CASE1. The initiation of convection in this case is created by forced convergence near the surface based on nudging the vertical velocity over the same volume that is used for the warm bubble in CASE1. The methodology is described in detail in Naylor and Gilmore (2012) and we use an updraft speed peaking at $5\,\mathrm{m\,s^{-1}}$ at the centre of the volume.

Both cases are simulated without a boundary layer scheme and the calculation of surface fluxes or radiation. The horizontal grid spacing of the simulations is 1 km to sufficiently resolve the main features of the simulated supercell. We use a model domain size of 84 grid cells in each horizontal dimension and open boundary conditions on each side of the modelling domain. The vertical resolution of the 96 model layers varies from about 50 m at the surface to 300 m at the top of the model. Simulations are performed with a time step of 5 s. The standard model diagnostics and the microphysical pathway diagnostics (Sect. 2.3) are output every 5 min to sufficiently resolve the development of the microphysical processes during the life cycle of the deep convective clouds.

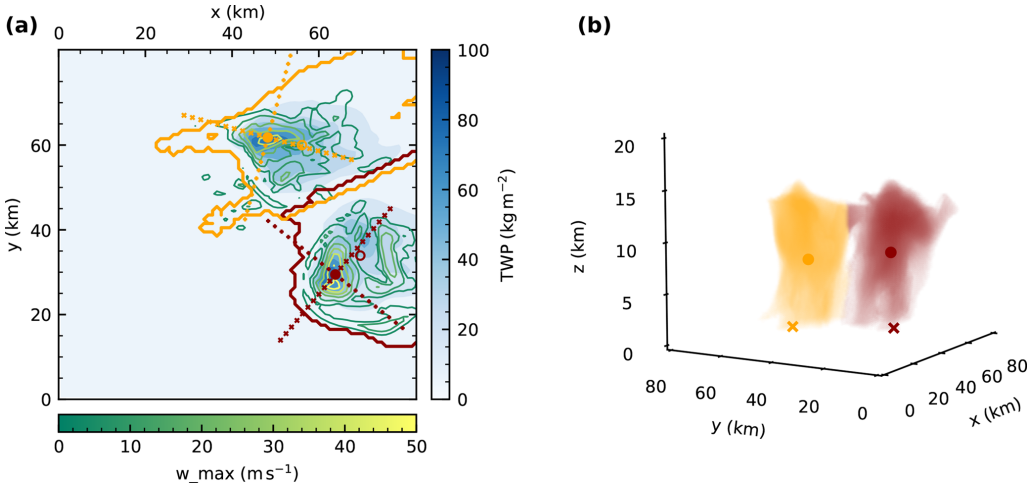

Figure 1. (a) Illustration of the result of the tracking and watershedding methodology after 90 min of simulation time with the total water path field in blues and contours of column maximum vertical velocities in greens. The filled circles represent the tracked updraft cores, while the empty circles show the position of the centre of gravity determined by the watershedding algorithm. Crosses denote the slices along/across the line of travel of the cell that are used for the analysis of the cloud morphology. The coloured contour lines represent the projection of the respective cloud mask for each cell to the surface. **(b)** Three-dimensional rendering of the 1 g kg^{-1} condensate mixing ratio threshold of the two tracked cells in the simulation at the same point in time, including the horizontal location of the tracked updraft (cross) and centre of gravity (dot).

2.2 Variation of aerosol proxies: CDNC or CCN

We analyse the effects of varying the CDNC in the two bulk microphysics schemes to isolate the impact of microphysical pathways. We use a CDNC of 250 cm^{-3} as a baseline simulation. Simulations are performed for two CDNC values corresponding to a cleaner environment than the baseline simulation (50 and 100 cm^{-3}) and five values representing more polluted conditions (500, 1000, 1500, 2000 and 2500 cm^{-3}).

For the simulations with the spectral-bin microphysics scheme, activation of aerosols to cloud droplets is calculated from a CCN spectrum following the equation $N_C = N_0 \cdot S^k$, with the prognostic supersaturation S, the particle number concentration N_0 and an exponent k. The exponent is kept fixed at $k = 0.5$, while N_0 is varied in a range from 75 to 6750 cm^{-3}. This yields cloud droplet number concentrations with median values spanning a similar range to those chosen for the two bulk microphysics schemes (Table 1).

2.3 Pathway analysis

We have extended two double-moment bulk microphysics schemes, the Morrison scheme (Morrison et al., 2005, 2009) and the Thomson scheme (Thompson et al., 2004, 2008) in WRF 3.7.1, by writing detailed microphysical pathway diagnostics at each output time step. This includes all individual process rates for both hydrometeor mass and hydrometeor number mixing ratio as well as individual latent heating rates for the three phase transitions (liquid–vapour, liquid–ice, ice–vapour) and the hydrometeor mass and number tendencies for the individual hydrometeor classes (cloud water, rain, cloud ice, graupel, snow) are diagnosed at every output time step.

For most analyses in this study, the individual microphysical processes are grouped into a consistent set of classes according to their contribution to the hydrometeor mass transfer in the model. This includes the six different phase transitions between frozen hydrometeors, water drops and water vapour (*condensation*, *evaporation*, *freezing* including riming, *melting*, *deposition* and *sublimation*) as well as the warm *rain formation* due to autoconversion and accretion of cloud droplets and all processes that transfer mass between the different frozen hydrometeors as *ice processes*. For some of the more detailed analyses, this grouping is performed in a more detailed way, e.g. separating freezing and riming processes or splitting them up by the specific hydrometeor class involved in the transfer. A collection of all the individual microphysical process rates represented in the two bulk microphysics schemes including the grouping discussed here is given in the Appendix (Table B1 for the Morrison microphysics scheme and in Table B2 for the Thompson microphysics scheme).

2.4 Convective cell tracking

We have developed a tracking algorithm focussed on the tracking of individual deep convective cells in CRM simulations, but flexible enough to be extended to other applications, e.g. simulations of shallow convection or based on geostationary satellite observations using brightness temperature data. The initial tracking of features is performed on the column maximum vertical velocity at each output time step using Python tracking library trackpy (Allan et al., 2016).

Table 1. Overview of the 52 simulations performed in this study, including the two cases simulated and the different CDNC/CCN values for each of the microphysics schemes. The CDNCs for the SBM simulations are the median values for grid points with a cloud water mixing ratio larger than $10\,g\,kg^{-1}$. Bold values of CDNC and CCN show parameters that were set in the simulation setup; the CDNC values for the SBM were diagnosed from the simulation results.

Case	Microphysics	CDNC (cm^{-3})	CCN (cm^{-3})
CASE1 Weisman and Klemp (1982, 1984)	**MORR** Morrison et al. (2005, 2009)	**50**, **100**, **250**, **500**, **1000**, **1500**, **2000**, **2500**	–
	THOM Thompson et al. (2004, 2008)	**50**, **100**, **250**, **500**, **1000**, **1500**, **2000**, **2500**	–
	SBM Khain et al. (2004) Lynn et al. (2005a, b)	12, 28, 54, 128, 419, 648, 870, 1310, 1753, 2194	**67.5**, **135**, **270**, **540**, **1350** **2025**, **2700**, **4050**, **5400**, **6750**
CASE2 Naylor and Gilmore (2012) Dawson et al. (2013) Kumjian et al. (2010)	**MORR** Morrison et al. (2005, 2009)	**50**, **100**, **250**, **500**, **1000**, **1500**, **2000**, **2500**	–
	THOM Thompson et al. (2004, 2008)	**50**, **100**, **250**, **500**, **1000**, **1500**, **2000**, **2500**	–
	SBM Khain et al. (2004) Lynn et al. (2005a, b)	12, 25, 47, 171, 393 603, 819, 1239, 1657, 2078	**67.5**, **135**, **270**, **540**, **1350** **2025**, **2700**, **4050**, **5400**, **6750**

These features are then filtered and linked to consistent trajectories. The trajectories are extrapolated to two additional output time steps at the start and at the end to allow for the inclusion of both the initiation of the cell and the decaying later stages of the cell development.

Based on these trajectories, a three-dimensional watershedding algorithm, *morphology.watershed* from the Python image processing package scikit-image (van der Walt et al., 2014), is applied to the total condensed water content field (mass mixing ratio of all hydrometeors) at each output time step to infer the volume of the cloud associated with the tracked updraft. We use a threshold of $1\,g\,kg^{-3}$ to define the core cloudy grid points in the simulations. A variation of this threshold by up to an order of magnitude to $0.1\,g\,m^{-3}$ only showed minor changes to the results of the study.

A separate watershedding is performed for both liquid water content (cloud droplets and rain drops) and ice water content (all ice hydrometeors). This allows for the determination of the centre of gravity and the mass, for the entire cloud as well as for the in-cloud liquid and frozen phases, respectively. The evolution of the centre of gravity has been studied mainly for warm convective clouds (e.g. Koren et al., 2009; Dagan et al., 2015, 2017, 2018) and with a focus on the warm phase of deep convective clouds (Chen et al., 2017).

The tracking algorithm does not explicitly treat splitting and merging of convective cells. In all simulated cases in this study, the initial convective cell splits into two separate counter-rotating cells early into the simulations. In CASE1 this leads to a relatively symmetric situation with similarly strong individual cells. In both cases, one of the cells develops more directly out of the initial cell: in CASE1 this is the right-moving cell, while in CASE2 this is the stronger left-moving cell. In each simulation, this stronger cell gets picked up as a continuation of the initial cell by the tracking algorithm. The second cell has been analysed following the same methodology and showed very similar results in all major aspects. We have thus decided to focus on the analysis of the first cell in this paper and to not discuss the results from the second cell in more detail.

Microphysical process rates, latent heating rates and other cloud microphysical parameters such as hydrometeor mixing ratios are summed up for regularly spaced altitude intervals in the volume of the individual cells to get representative profiles for each cloud. We interpolate the microphysical process rates and other variables used in the analysis to slices along and perpendicular to the line of travel of the cell (Fig. 1) to visualise and analyse the morphology of the cells for different simulation set-ups and at different stages of the cloud life cycle.

3 Results

3.1 Baseline simulations

The simulations with $CDNC = 250\,cm^{-3}$ for both bulk microphysics schemes (Figs. 2 and 3) are used as a baseline simulation representative of intermediate aerosol loading. As for all the following figures for CASE1, these analyses are based on a combination of the initial stage of the cell and the right-moving cell after the cell split. We use three different points in time (15, 25 and 60 min) to illustrate the microphys-

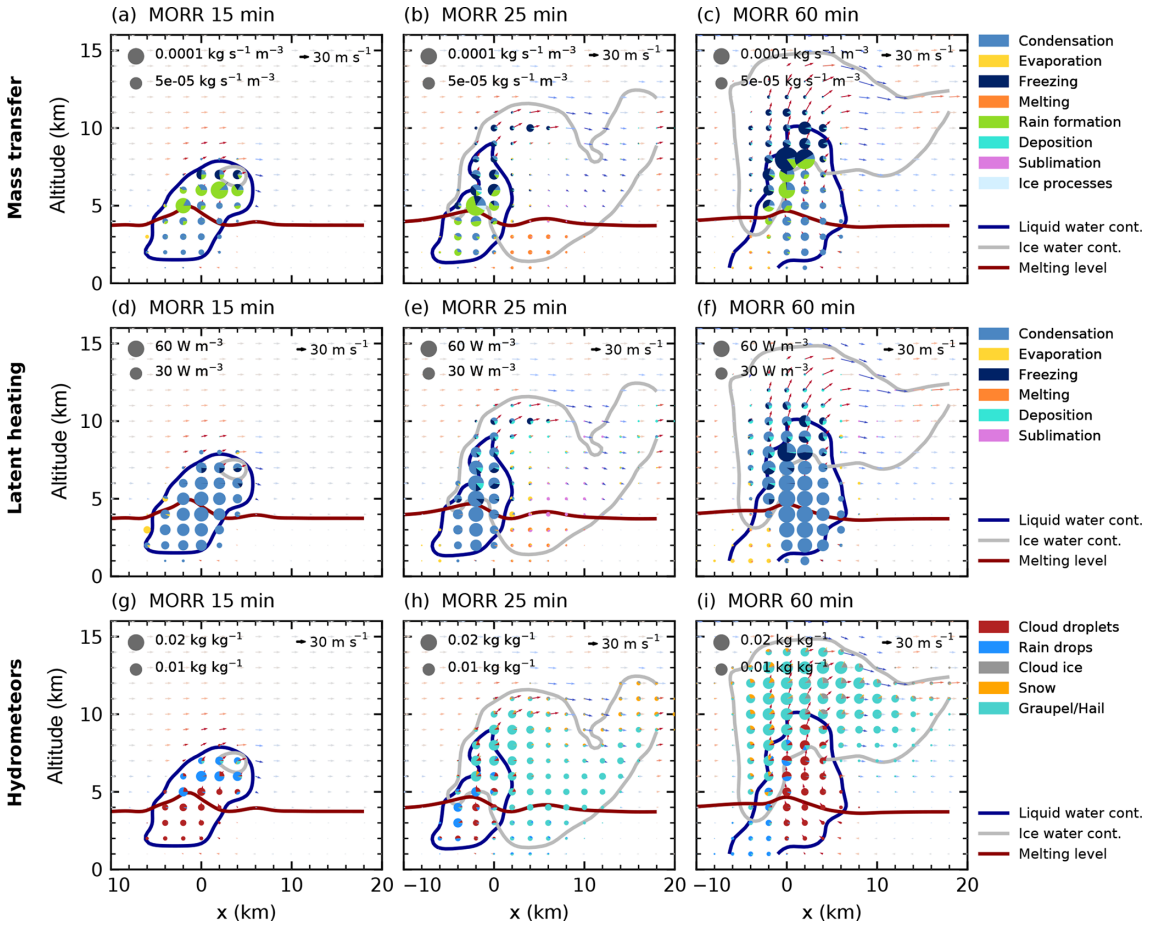

Figure 2. Cloud microphysical morphology along a slice parallel to the cell track for a cloud droplet number concentration of 250 cm^{-3} for the Morrison microphysics scheme. The area of each specific colour in the pie charts is proportional to the water turnover **(a)–(c)** in $kg\,m^{-3}\,s^{-3}$ and latent heating **(d)–(f)** in $W\,m^{-3}$ for the process rates and to the mass mixing ratio for the hydrometeors **(g)–(i)**. Contour lines denote the mixing ratio threshold of 1 $g\,kg^{-1}$ for liquid (blue) and frozen (grey) water content as well as the melting level (0 °C isotherm). Arrows denote the wind field with updrafts in red and downdrafts in blue.

ical evolution of the cell in simulations with the two different microphysics schemes.

During the initial phase of the formation of the convective cloud in the simulation using the Morrison bulk microphysics scheme (Fig. 2a, d, g), the two major microphysical processes are condensation to form cloud droplets and rain formation from these droplets, while the top of the cloud at around 7.5 km is already influenced by freezing and riming processes. The simulation with the Thompson microphysics scheme shows a similar development during the initial cloud stage (Fig. 3a, d, g). The initiation of freezing at the top of the cloud is slightly delayed in comparison to the simulation with the Morrison scheme. During the next 10 min, the cell quickly intensifies, dominated by the development of rain formation (autoconversion of cloud droplets and accretion of cloud droplets by rain) between 4 and 7 km. Freezing occurs at a height of about 7–8 km. After an hour of simulation, the cell has developed into a mature supercell with hail dominating the mass mixing ratio in the ice phase. A significant amount of cloud droplets extends up to 10 km height. Rain formation and freezing occur in the region of the strongest updraft with a width of about 5 km for both microphysics schemes. During the later stage, the freezing in the simulation using the Morrison microphysics scheme takes place over a substantial vertical range and is strongest at both edges of the mixed-phase region of the cloud at around 8 and 10 km altitude (Fig. 2c). The Thompson scheme instead shows a more confined region of freezing. In both bulk microphysics schemes, condensation processes dominate the latent heat release in the cloud for all stages of the cloud development (Figs. 2d–f, 3d–f). In the mature stage of the cell, the main difference in the hydrometeor classes between the two microphysics schemes is an enhanced presence of snow both in the core and in the anvil for the Thompson microphysics scheme (Figs. 2i and 3i).

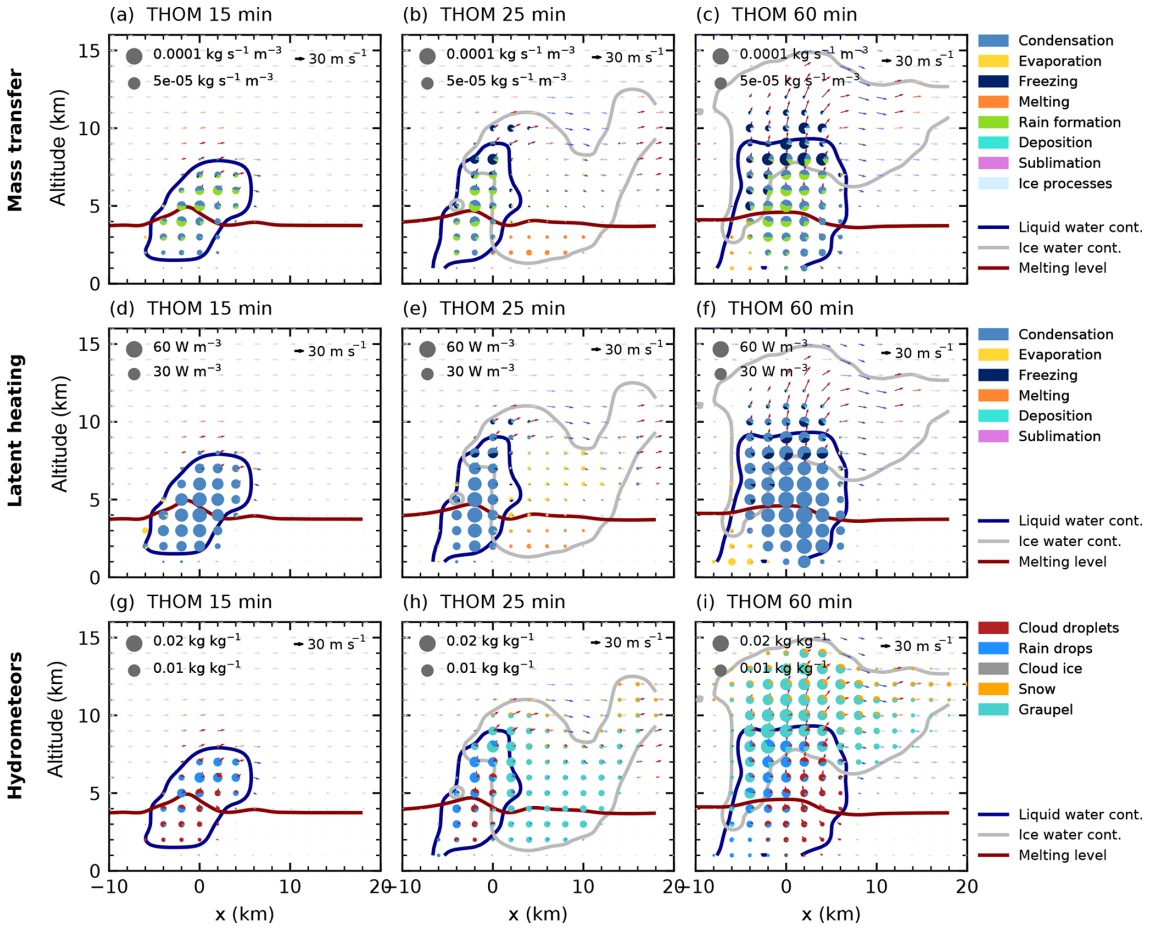

Figure 3. Cloud microphysical morphology along a slice parallel to the cell track for a cloud droplet number concentration of 250 cm^{-3} for the Thompson microphysics scheme as in Fig. 2.

3.2 Effects on cloud morphology and microphysical process rates

We first investigate changes to the right-moving cell in CASE1 due to a variation of CDNC. We focus on three different CDNC values (clean, baseline, polluted; see Fig. 4) after 60 min of simulations using the two bulk microphysics schemes. In the microphysical process rates, a decrease in rain formation from droplets (autoconversion and accretion) with increasing CDNC is evident in the core of the cell for both bulk microphysics schemes. For both bulk schemes, the freezing and riming processes are shifted upwards with increasing CDNC. The mixed-phase region of the cloud, indicated by the liquid water mixing ratio contour in Fig. 4, extends about 1–2 km higher in the polluted case for each bulk scheme.

In the hydrometeor mass mixing ratios (Fig. 5), an increase in cloud droplet mass at the expense of raindrops for increasing CDNC is evident in both bulk microphysics schemes and the spectral-bin microphysics scheme, particularly in the mixed-phase region of the cloud at around 6–8 km. In the Thompson scheme, most of the ice-phase hydrometeor mass is present in the form of snow for the high CDNC simulation (Fig. 5d), especially towards the cloud top and in the anvil region, while graupel dominates except in the anvil for the cleanest case (Fig. 5c). In contrast, the ice phase in the Morrison scheme shows a high hail mixing ratio for low and high CDNC values (Fig. 5a, b) and additional ice particles, but only small amounts of snow in the simulation with the highest CDNC value. The simulations using the spectral-bin microphysics scheme (Fig. 5e, f) show a stronger increase in cloud droplet mass mixing ratio than the two bulk schemes for increased CCN. Graupel and hail, the predominant ice-phase hydrometeors in the cleanest simulation, get replaced by cloud-ice particles for the highest CCN value. However, it has to be taken into account that the definition of the hydrometeor classes differs between the three different microphysics schemes.

Figure 6 provides a vertically resolved view of the time evolution of the microphysical process rates over the life cycle of the right-moving cell for the two bulk microphysics schemes under the cleanest and most polluted conditions. For

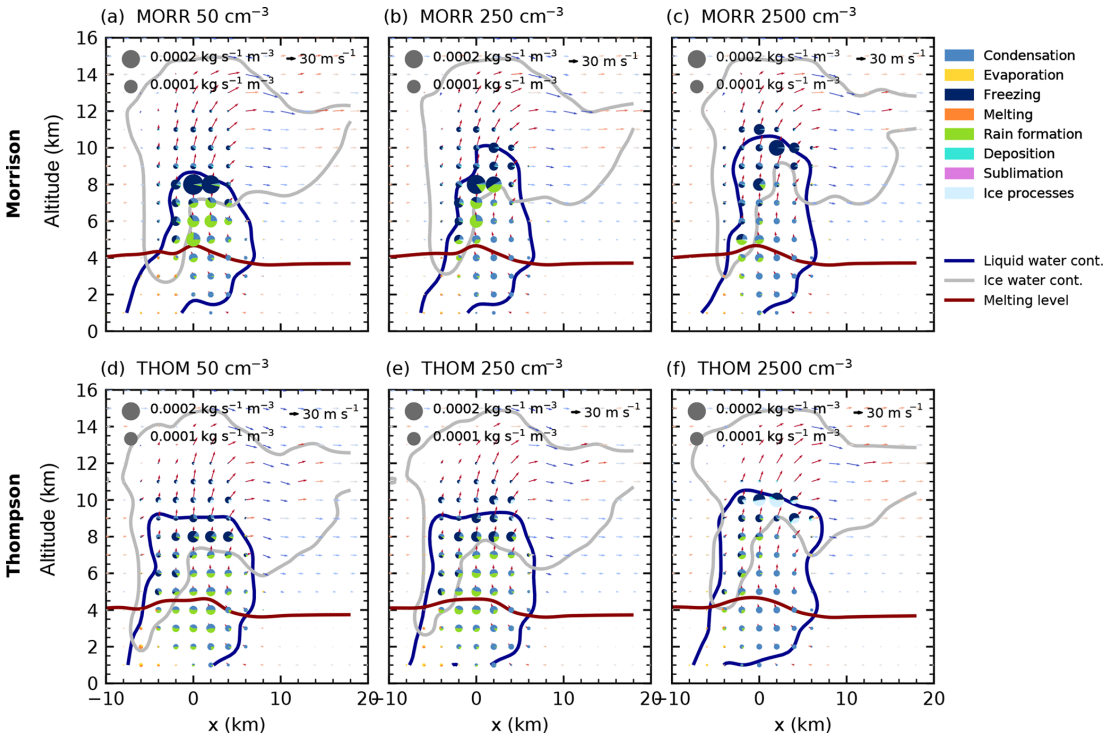

Figure 4. Cloud microphysical morphology along a slice through the cloud parallel to the track of the cell for simulations with three different CDNC values (**a, d**: 50 cm^{-3}, **b, e**: 2500 cm^{-3}, **c, f**: 2500 cm^{-3}) after 60 min of simulation using the two bulk microphysics schemes (**a–c**: Morrison, **d–f**: Thompson).

both schemes, a strong decrease in the warm rain formation processes (autoconversion of cloud droplets and accretion of cloud droplets by rain) with increased CDNC can be observed. This even leads to a complete shut-down of warm rain production in the Thompson scheme, which is also evident in the absence of rain hydrometeors in Fig. 4. As a result, evaporation in the lowest model levels decreases strongly for the high CDNC value in the simulations with the Thompson scheme. Both microphysics schemes show a significant decrease in the total amount of melting of frozen hydrometeors below the melting line at about 4 km height. The strong cooling due to evaporation and melting in the cleanest cases for the simulations with the Thompson scheme (Fig. 6c) can explain the significantly shorter lifetime of the cell compared to the more polluted cases and the other bulk scheme. The dominant region of freezing processes is lifted from around 8 km height in the low CDNC case to around 10 km for the high CDNC case height in both schemes. While deposition on ice hydrometeors is a significant process for all values of CDNC for the Morrison scheme, it becomes more enhanced for the most polluted simulation using the Thompson scheme, related to the change in the dominant ice-phase hydrometeor class to snow (Fig. 5). Condensation onto cloud droplets is present in all simulations up to 10 km height in comparable amounts and dominates the latent heating due to the large energy transfer involved. Deposition processes onto ice hydrometeors are significant for both the cleanest and the most polluted simulation in the Morrison scheme, while the Thompson scheme shows much more deposition in the most polluted case, which can be related to the changes in the hydrometeor composition (Fig. 5). The decrease in the total amount of microphysical mass transfer in all simulations around 55 min into the simulations is caused by the splitting of the tracked cell into two individual cells. However, no significant change to the relative proportions of the different processes can be observed at this stage.

A more detailed analysis of the processes involved in the formation of rain over the lifetime of the cell in the different cases (Fig. 7) reveals that autoconversion of cloud droplets to rain for the highest CDNC values in both bulk schemes is almost negligible, with only very little autoconversion in the Morrison scheme, even for the smallest CDNC value. Accretion of cloud droplets by rain is strongly depressed for high CDNC in both microphysics schemes. Melting of ice hydrometeors contributes significantly to the production of rain in both bulk schemes and is reduced for the high CDNC case, especially in the Thompson scheme.

The processes transforming liquid to frozen water can be further broken down into processes representing the freezing of individual cloud droplets or raindrops and riming processes, in which existing ice-phase hydrometeors accrete liquid water (Fig. 8). For both bulk microphysics schemes,

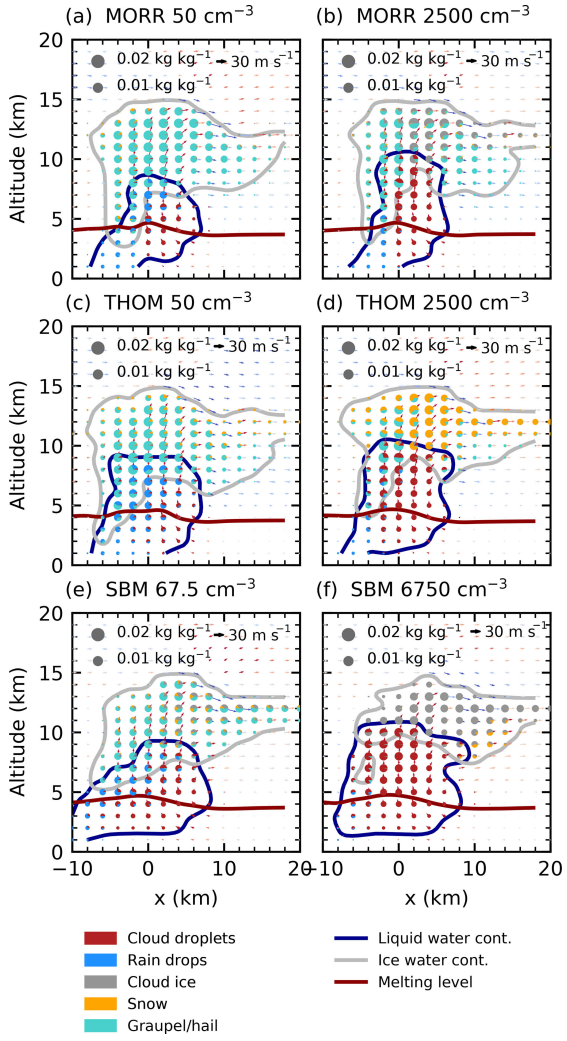

Figure 5. Hydrometeor mass mixing ratios in a slice along the line of travel of the cell for the cleanest **(a, c, e)** and most polluted **(b, d, f)** simulations after 60 min of simulation for the three microphysics schemes in CASE1.

freezing of raindrops and cloud droplets occurs in two separate layers, with freezing of raindrops at around 8 km and freezing of cloud droplets above a height of 10 km up to 14 km. In both microphysics schemes, freezing of raindrops is strongly decreased for increased CDNC (Fig. 8b, d), while freezing of cloud droplets is increased by about a factor of 3. This is not related to the parameterisation of the freezing processes (described in more detail in Appendix B), which does not include any information about cloud droplet effective radius and raindrop effective radius through the number concentrations. Instead, these changes are purely a result of the shift in the abundance of cloud droplets and raindrops (Fig. 5).

The riming processes are spread out over a much larger altitude range in the cloud, between the melting level at about 4 km and about 11 km height for riming of cloud droplets and below 9 km for the riming of raindrops. Riming is significantly stronger at all CDNC values in the simulations with the Morrison scheme (Fig. 8a, b). In the Morrison scheme, riming of rain droplets is strongly decreased for higher CDNC and mainly restricted to around 5 km height. In the Thompson microphysics scheme (Fig. 8c, d), raindrop riming is also strongly decreased for high CDNC, but still occurs over the same height range as in the low CDNC case. Both microphysics schemes show a slight increase in droplet riming with higher CDNC over the entire altitude range. We can thus explain the shift in freezing and riming processes observed in Fig. 6 by a decreased riming of rain droplets at lower altitudes and a shift from the freezing of raindrops to the freezing of cloud droplets occurring at higher altitudes.

The evolution of the deposition and sublimation processes (Fig. 9) shows substantial differences between the two bulk microphysics schemes and a strong response to a variation of CDNC. The calculation of deposition and sublimation in the microphysics scheme is explicitly parameterised for each hydrometeor class, taking into account detailed information on the size distribution of the hydrometeors (Thompson et al., 2004; Morrison et al., 2005). In the Morrison scheme (Fig. 9a, b), the increase in CDNC leads to a decrease in both deposition and sublimation over the entire height of the cloud. These processes dominantly occur on hail for the cleanest case and are more distributed over hail, snow and pristine ice in the polluted case, which agrees with the shifts in the hydrometeor mixing ratios (Fig. 5a, b).

In the simulations with the Thompson microphysics scheme (Fig. 9c, d), deposition and sublimation processes show a very different behaviour. The strong increase in snow in the cloud with increasing CDNC (Fig. 5c, d) leads to a strong increase in both deposition and sublimation on snow. Deposition on ice is of the same order of magnitude for the cleanest case, but is not strongly affected by a change in CDNC. Sublimation of graupel only occurs around and below the melting layer and is significantly reduced by increasing CDNC. As deposition on graupel is prohibited in this microphysics scheme, there is no decrease in deposition on graupel associated with the changes in the hydrometeor ratio compensating the increase in deposition on snow. This leads to a strong increase in total deposition with increased CDNC as the main response in the Thompson scheme.

Latent heating constitutes a key feedback of the microphysics scheme onto the model dynamics along with changes to the buoyancy due to changes in condensate loading. The vertically resolved latent heating over the lifetime of the tracked cell in CASE1 is shown in Fig. 10 for all three microphysics schemes and split up into the individual phase changes for the two bulk microphysics schemes in Fig. 11.

Latent heat release from condensation is the dominant contribution to the latent heating and about a magnitude stronger than the other contributions, thus determining the general shape of the latent heating profile (Figs. 10 and 11a, g). The changes to condensation due to changes in CDNC in the two

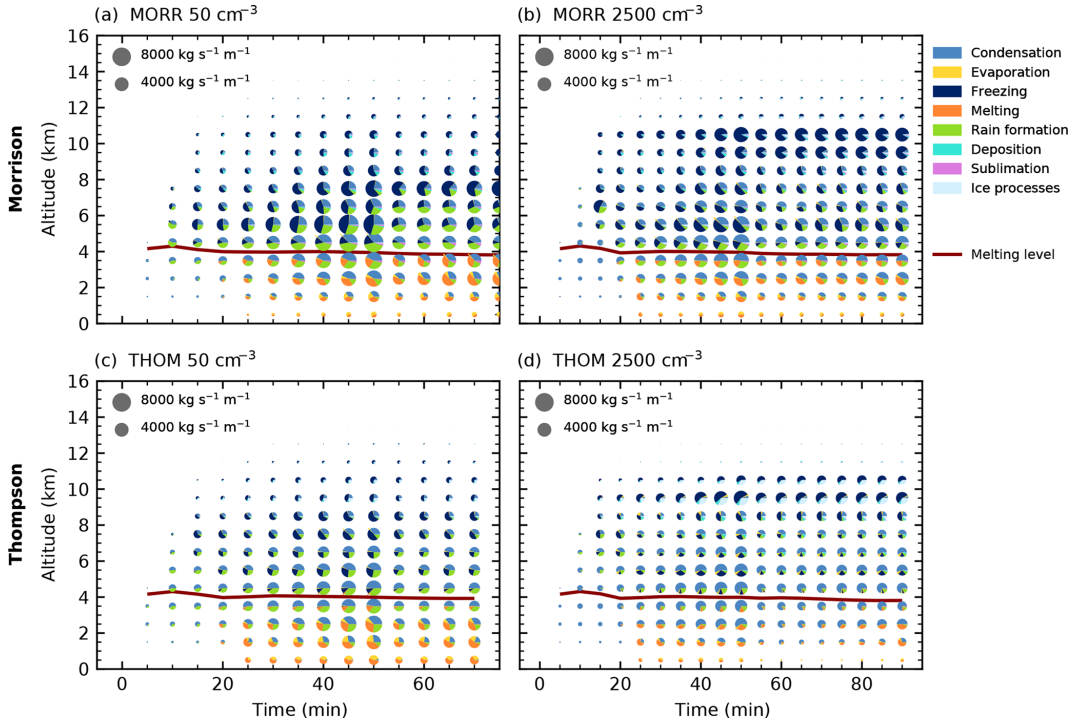

Figure 6. Time evolution of the microphysical process rates for the cleanest **(a, c)** and most polluted **(b, d)** simulations and the two bulk microphysics schemes (Morrison: **a, b**, Thompson: **c, d**) in CASE1. The pie charts denote mass transfer summed up over the volume of the cloud in each altitude interval for the different groups of microphysical process rates with the area of each colour proportional to the mass transfer. The red line shows the height of the 0 °C isotherm.

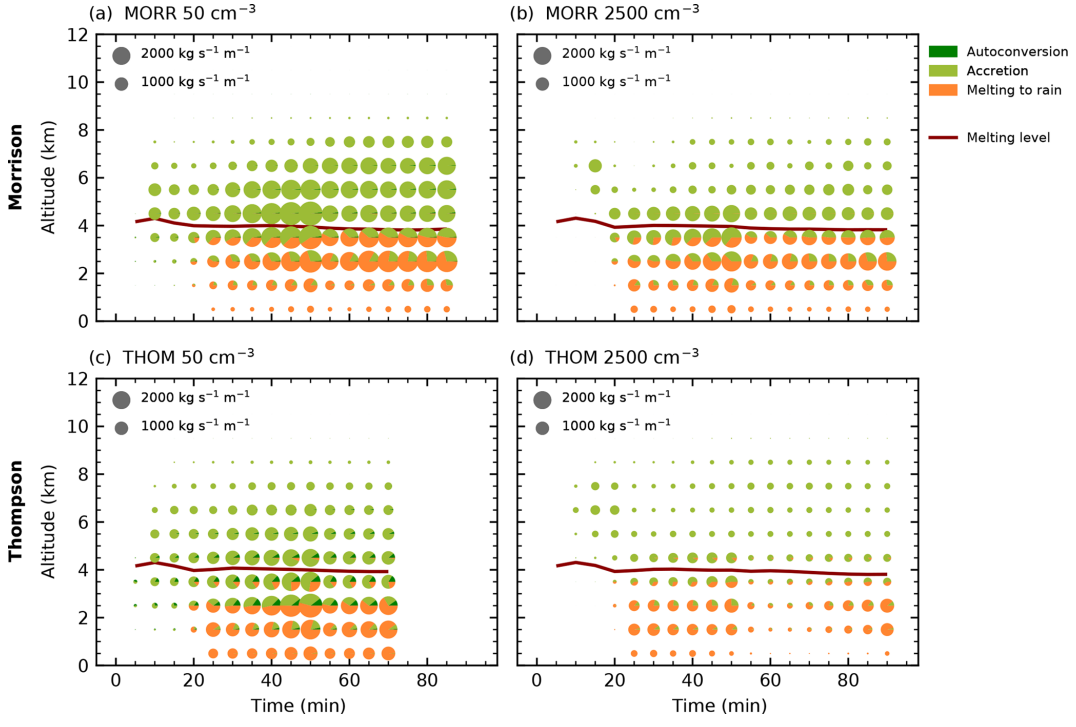

Figure 7. Time evolution of the microphysical process rates relevant for rain formation processes (autoconversion, accretion of cloud droplets by rain and melting of ice hydrometeors) as in Fig. 6.

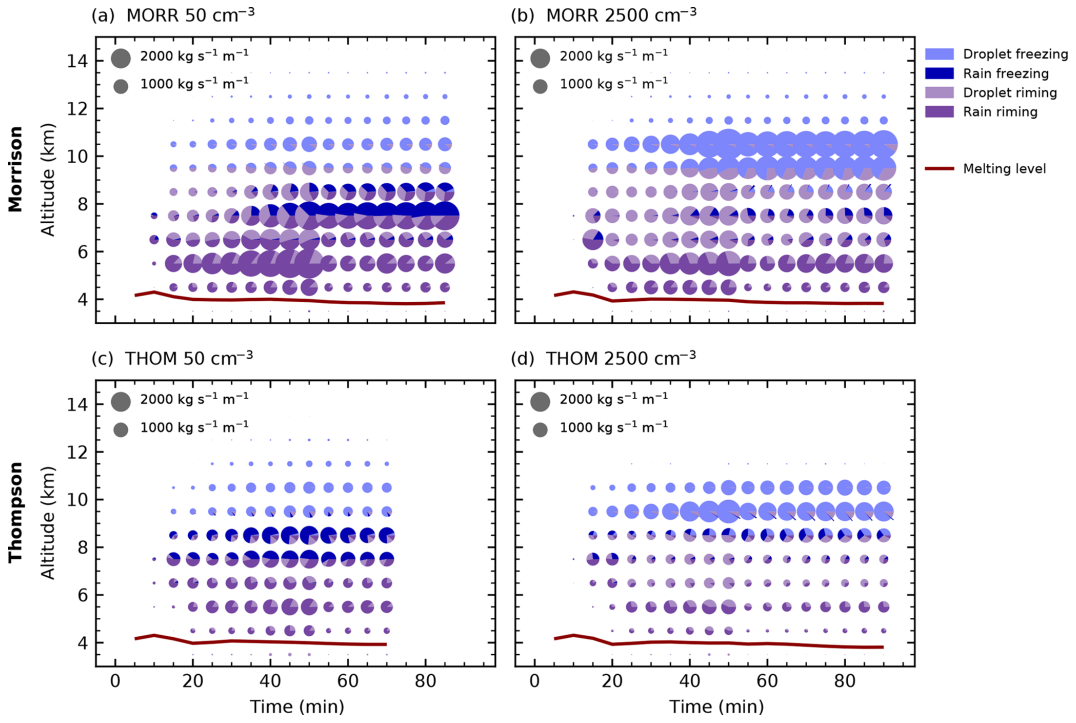

Figure 8. Time evolution of the microphysical process rates of freezing and riming processes as in Fig. 6.

bulk microphysics schemes are comparatively small, which can be explained by the use of saturation adjustment in the calculation of the condensation, which does not include an effect of changes in droplet radius on the condensation.

The same limitation applies to the evaporation of cloud droplets, which also cannot show any direct effect from changes in CDNC due to the use of saturation adjustment. However, the evaporation shows much stronger differences between the two microphysics schemes and also a stronger effect of a variation in CDNC (Fig. 11b, h). The strong changes in the evaporation at higher levels in the mixed-phase region of the cloud, especially for the Thompson scheme, can be explained with the changes in deposition on frozen hydrometeors (Fig. 11e, k). The increased deposition with increasing CDNC through the changes to the frozen hydrometeors could lead to a further decrease in the saturation vapour pressure over water in the water-subsaturated regions of the cloud and thus additional evaporation. There is also a noticeable decrease in condensation in the higher layers of the mixed-phase region of the cloud at around 10 km for the Thompson scheme (Fig. 11g), which could be similarly related to the increase in deposition. The evaporation in the lower layers is associated with the evaporation of raindrops. The differences between the two schemes and the variation with changes in CDNC can be directly related to the differences in the amount of rain, which is both higher and more strongly decreasing with increasing CDNC in the Thompson scheme than in the Morrison scheme.

All three microphysics schemes show a small shift of latent heating to higher altitudes superimposed on that in the range between 7 km and about 10 km for increasing CDNC (Fig. 10), which can be associated with the shifts in freezing and riming (Fig. 11d, i), described in more detail in Fig. 8. The decrease in latent cooling from melting processes in the lowest layers is stronger in the Thompson scheme than in the Morrison scheme (Fig. 11b, h).

There are large differences between the microphysics schemes in the latent heating and cooling from sublimation and deposition and their response to changes in CDNC. The Morrison scheme shows a significant decrease in both sublimation and deposition with increased CDNC (Fig. 11e, f). Apart from changes due to the shift in hydrometeors from hail to snow and cloud ice (Figs. 5 and 9), these decreases can be related to the lower amount of ice hydrometeors in the mixed-phase region of the cloud. Although these two changes cancel each other to a large extent in the integrated latent heating, the two processes occur at different heights, which results in a shift of latent heating to lower levels, opposing the changes to the freezing and riming processes (Fig. 11c). Furthermore, this strong decrease in sublimation leads to a decrease in water vapour near the cloud base, which could cause the consistent decrease in condensation at around 5 km altitude in the Morrison scheme (Fig. 11a).

In the Thompson scheme, sublimation of ice hydrometeors is weak and barely affected by changes in CDNC (Fig. 11l). However, increases in CDNC lead to an increase in deposition in the higher parts of the cloud (Fig. 11k). This effect

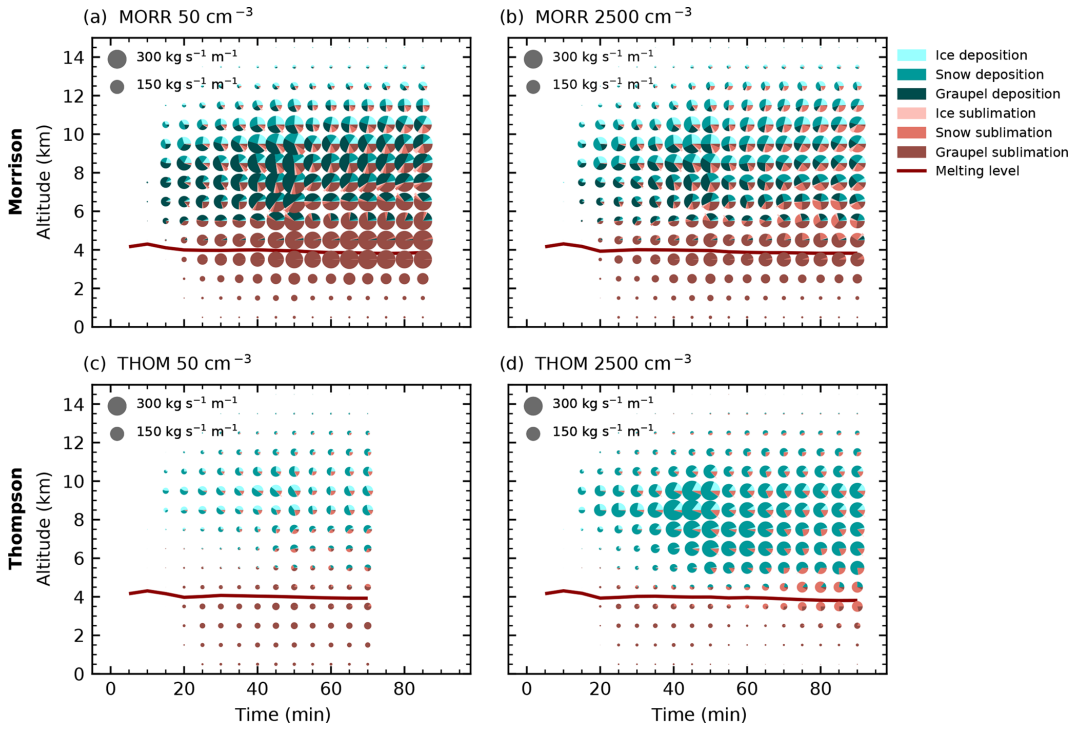

Figure 9. Time evolution of the microphysical process rates of deposition and sublimation as in Fig. 6.

can be explained by the observed shift in hydrometeors from graupel to cloud ice and snow since deposition on graupel is turned off in the Thompson microphysics scheme, while it occurs on both snow and cloud ice. This increase in deposition could be the main reason for the changes observed in evaporation of cloud droplets as it significantly increases the sub-saturation over water in the mixed phase in regions that are supersaturated with respect to ice. This can be interpreted as a manifestation of the Wegener–Bergeron–Findeisen process (Wegener, 1911; Findeisen, 1938; Findeisen et al., 2015; Storelvmo and Tan, 2015), transferring water mass from liquid hydrometeors to the frozen hydrometeors. This constitutes an additional feedback from the changes in the ice phase back onto the liquid-phase hydrometeors.

In contrast to the increased latent heating from freezing or melting, changes in condensation and evaporation, as well as in sublimation and deposition, are linked to a change in condensate loading, which affects the buoyancy of the cloud and thus at least partially buffers the impact of latent heating and cooling on the dynamics of the clouds.

The changes to the vertically integrated latent heating in the cloud for all three microphysics schemes do not show a significant trend with increasing CDNC (Fig. 10d, e, f). The Thompson scheme shows slightly higher integrated latent heating for the two simulations with the highest CDNC content but no consistent trend over the rest of the simulations (Fig. 10e). The SBM simulations show a slightly decreasing trend of integrated latent heating for the highest CDNC values above 1000 cm^{-3} but no consistent trend over the entire range of values (Fig. 10f). Despite the significant change to the altitude of freezing, there is no systematic change in the integrated latent heat release from freezing for both bulk microphysics schemes that would contribute to an invigoration of the cloud. In the Morrison scheme, the strong changes in deposition and sublimation almost entirely cancel out when integrated vertically. In the Thompson microphysics scheme, the increase in the integrated latent heat release from deposition cancels out the significant decrease in the integrated evaporation of cloud droplets and rain.

3.3 Effects on cloud mass and centre of gravity

The tracking and watershedding allow for a determination of the cloud mass inside the identified cloud volumes and the centre of gravity of the hydrometeors in the cloud. These analyses are also performed separately for the liquid-phase and ice-phase hydrometeors in the cloud, which allows us to relate the changes in the properties for the entire cloud to changes in the individual phases.

The evolution of the cloud mass and the mass of the two water phases in the cloud (Fig. 12) in the three microphysics schemes is similar, with a maximum cloud mass of about 2×10^{10} kg for all microphysics schemes before the splitting of the cell and then about 1.5×10^{10} kg for the two bulk microphysics schemes (Fig. 12a, b) and slightly higher cloud masses of up to 1.8×10^{10} kg in the spectral-bin microphysics scheme (Fig. 12c). The cloud mass and also the difference

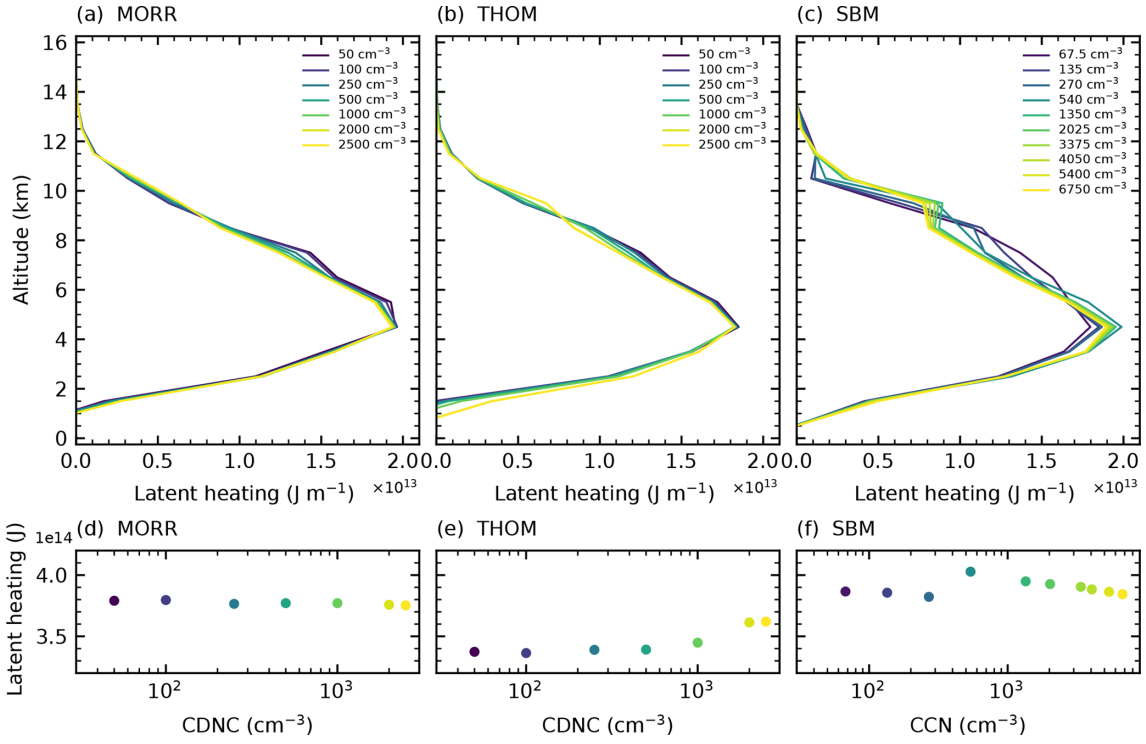

Figure 10. Profiles of the sum of latent heating over the lifetime of the dominant tracked cell for the three microphysics schemes in CASE1.

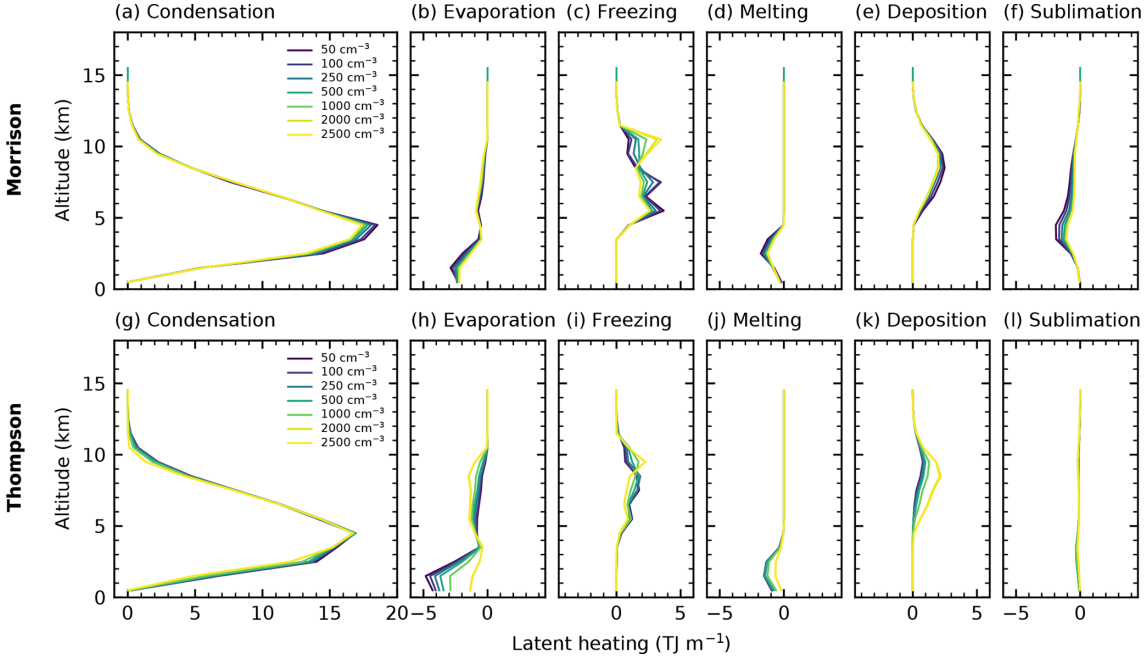

Figure 11. Profiles of the components of the latent heating and cooling over the lifetime of the tracked cell for the two bulk microphysics schemes in CASE1.

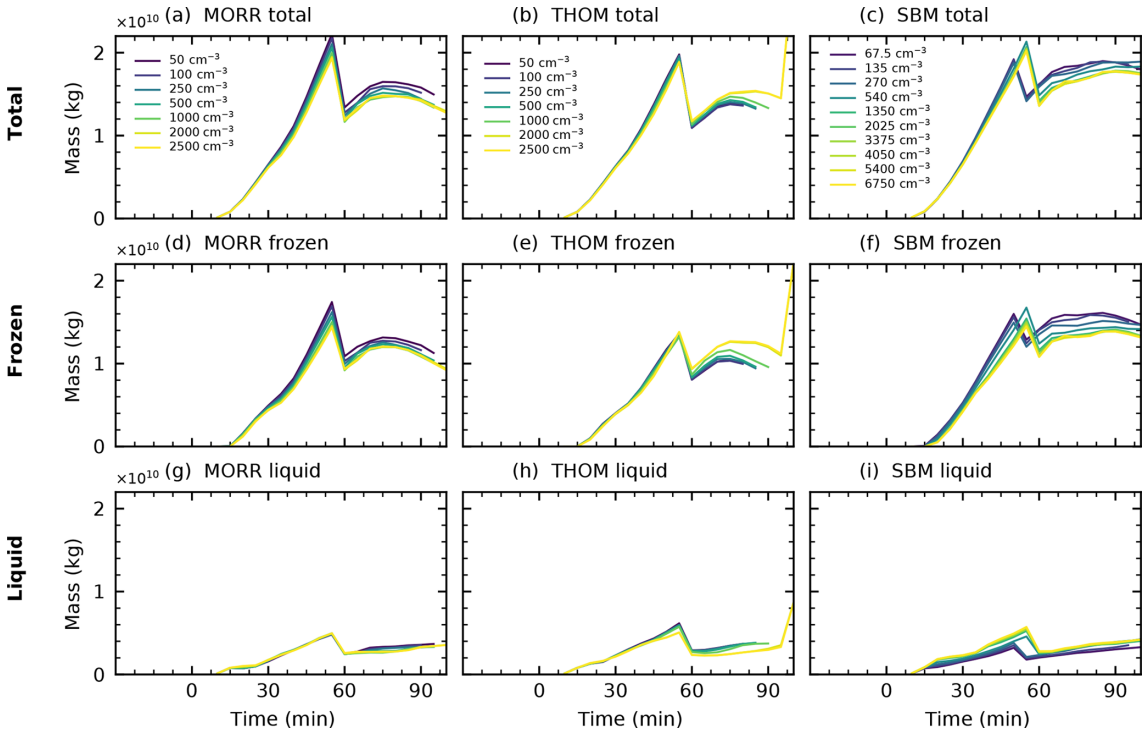

Figure 12. Total water mass, liquid water mass and frozen water mass in the analysed right-moving cell for the three different microphysics schemes (Morrison: **a**, **d**, **g**, Thompson: **b**, **e**, **h**, SBM: **c**, **f**, **i**) in CASE1. The jump in the curves occurs at the point where the cell splits into two individual cells.

between the bulk schemes and the bin scheme are dominated by the ice-phase hydrometeors, while the liquid-phase mass is very similar in all three different microphysics schemes, making up about 20 %–25 % of the total cloud mass.

There are, however, marked differences in the response to changes of the aerosol proxy between the microphysics schemes. The Morrison scheme shows a decrease in total cloud mass and ice-phase mass by about 10 %–15% over the range in which we increase the CDNC and no significant changes in the liquid phase. This decrease in ice-phase mass can be directly linked to the changes in the microphysical process rates analysed in Sect. 3.2. The shift of freezing to higher altitudes leads to a reduction in frozen hydrometeors in the mixed phase of the cloud and thus significantly less growth of the ice phase through vapour deposition. In the Thompson scheme, however, increased CDNC leads to an increase in ice-phase and total mass and a small increase in cloud liquid mass. This increase agrees well with the increased deposition due to the changes in the ice hydrometeor partition in the cloud discussed in Sect. 3.2. In the simulations using the SBM scheme, the two phases show a differing response to the aerosol proxy with increased liquid hydrometeor mass and a decrease in ice-phase mass for increasing CCN.

The altitude of the centre of gravity is affected by the choice of microphysics scheme, with an overall higher centre of gravity for the SBM scheme (Fig. 13c) compared to the two bulk microphysics schemes (Fig. 13a, b).

There is a consistent response in the cloud heights for all three microphysics schemes. The microphysics schemes show an increase in the height of the centre of gravity of the entire cloud, which is more pronounced using the Thompson scheme (about 1.5 km) than in the Morrison scheme (about 0.5–1 km). This includes an upward shift in both the liquid and frozen water in the cloud. The increased height of the liquid phase can be directly related to the decrease in the formation of warm rain (Fig. 6) and the more numerous cloud droplets reaching higher up in the cloud in the polluted case compared to the dominating raindrops in the cleanest case (Fig. 5). The increase in the altitude of the ice phase in the cloud with increased CDNC can be related to the changes in the altitude of the freezing processes. However, it can also be a result of the lower fall speeds of the ice and snow hydrometeors dominating in the polluted case instead of graupel and hail in the cleanest cases. As for the bulk microphysics schemes, there is an increase in the height for both phases in the simulations using the SBM scheme, which is significantly more pronounced in the liquid phase of the cloud.

All three microphysics schemes show a clear saturation in the effect of changes in the CDNC/CCN concentration. Variations above 2000 cm^{-3} in the bulk schemes and above 1350 cm^{-3} in the SBM simulations only lead to insignificant

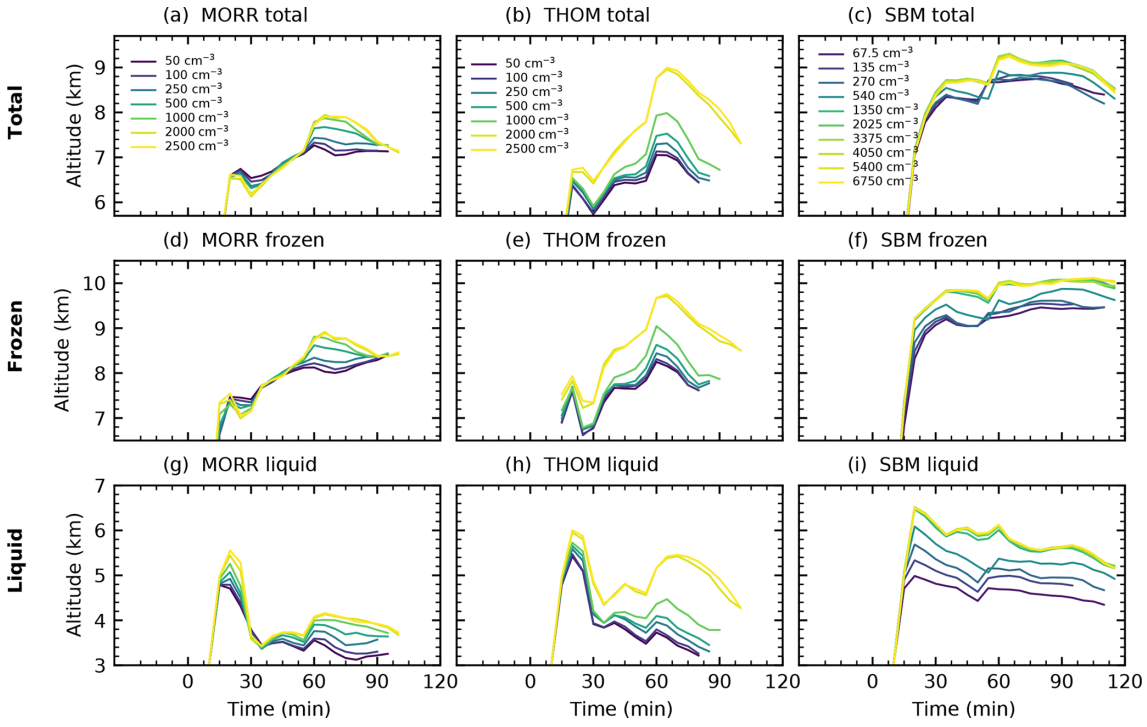

Figure 13. Altitude of the centre of gravity of the cloud and the individual phases in the analysed right-moving cell for the three different microphysics schemes (Morrison: **a**, **d**, **g**, Thompson: **b**, **e**, **h**, SBM: **c**, **f**, **i**) in CASE1.

effects on both the cloud mass and the altitude of the centre of gravity of the different phases.

3.4 Sensitivity test: a second idealised supercell case (CASE2)

To investigate the representativeness of the results and the response of the deep convective clouds to the variation of aerosol proxies CDNC and CCN, the same set of simulations and analyses have been performed for a second idealised supercell case (CASE2) with different forcing and initial conditions (Sect. 2.1).

The time evolution of the cloud-averaged process rates for the two bulk microphysics schemes (Fig. 14) shows that the total microphysical water transfer is much weaker in CASE2 than in CASE1, with process rates about a factor of 3 smaller. This case shows much stronger differences between the two bulk microphysics schemes in the general evolution of convection. For the Morrison microphysics scheme, a development of the convective cloud in two stages occurs. After an initial maximum in the microphysical processes after around 30 min of simulation time, the convective activity becomes weaker before picking up again after about an hour of simulation time. For the Thompson microphysics scheme, this second episode of development in the tracked cell is completely absent for all simulations, with the cloud dissipating after about 60 min of simulation time. This is potentially related to the substantially higher cooling at and below cloud base due to the evaporation of rain and the melting of frozen hydrometeors. The cooling can substantially weaken the convective updraft and thus prevent the further development of the cell that takes place in the simulations using the two other microphysics schemes. This finding agrees with a substantially shorter lifetime of the cleanest case for the simulations with the Thompson scheme in CASE1 (Fig. 6).

Despite these differences in the evolution, CASE2 shows very similar changes in the microphysical processes due to a variation of CDNC to CASE1 for both microphysics schemes. The formation of rain due to autoconversion of cloud droplets and accretion by rain is smaller and restricted to lower heights in the polluted case using the Morrison microphysics scheme. For the Thompson microphysics scheme, the formation of rain is decreased and shifted to higher levels in the model under polluted conditions. Furthermore, the freezing and riming processes predominantly occur at higher altitudes than in the clean case for both bulk microphysics schemes.

In line with these changes to the microphysical process rates, the evolution of the cloud mass in CASE2 (Fig. 15) is smaller than in CASE1 for the two bulk microphysics schemes, with about half as much hydrometeor mass in the cloud up to about 5×10^9 kg. The ice phase is more dominant, with the liquid phase of the cloud only accounting for less than a quarter of the total cloud mass. The simulation with the spectral-bin microphysics scheme shows a larger cloud mass than the two bulk schemes for this case,

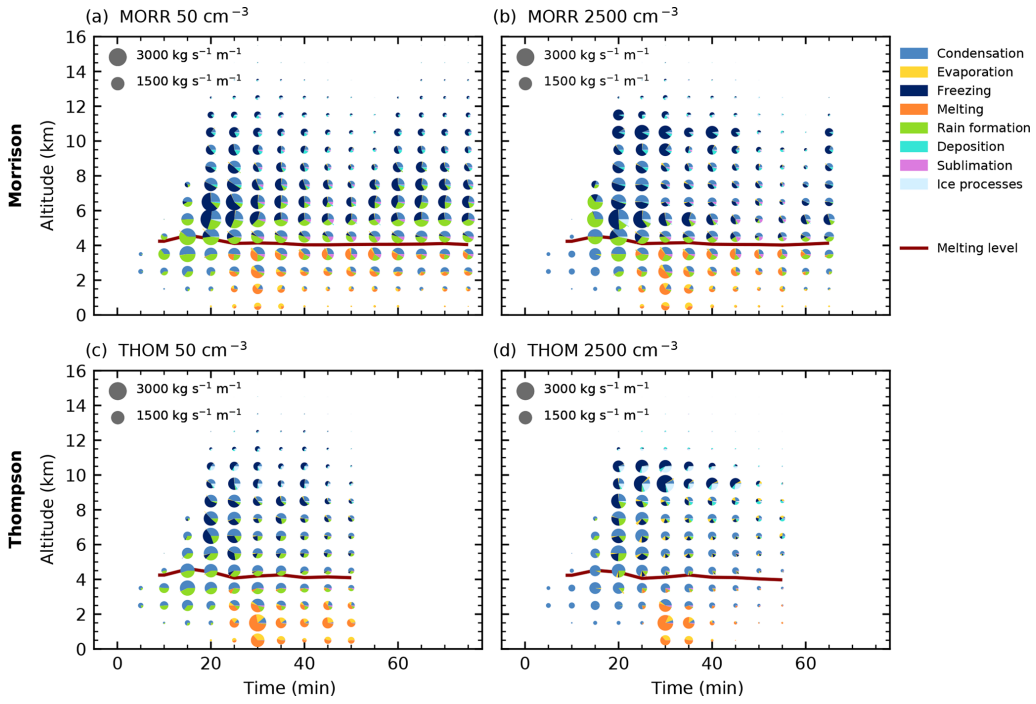

Figure 14. Temporal evolution of the microphysical process rates in CASE2 for the cleanest **(a, c)** and most polluted **(b, d)** simulations and the two bulk microphysics schemes (Morrison: **a**, **b**, Thompson: **c**, **d**). The pie charts denote the different groups of microphysical process rates with the area proportional to the sum of the microphysical process rates in the specific altitude interval inside the cloud volume.

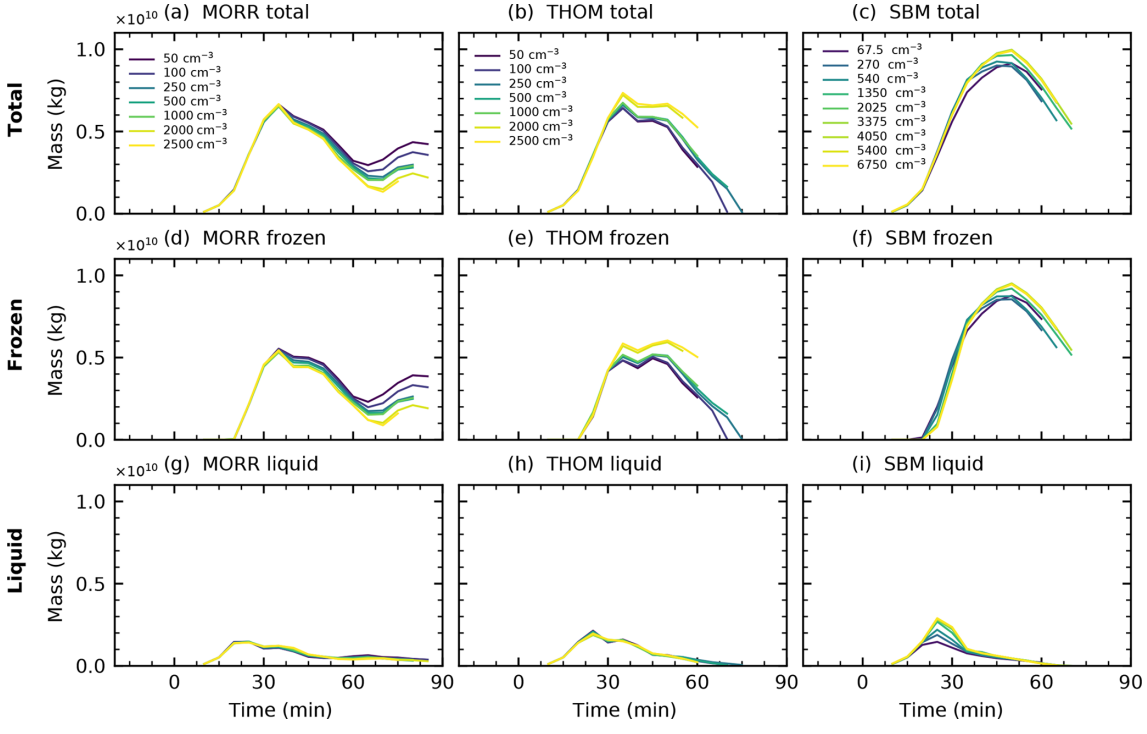

Figure 15. Total water mass, liquid water mass and frozen water mass in the analysed left-moving cell for the three different microphysics schemes (Morrison: **a**, **d**, **g**, Thompson: **b**, **e**, **h**, SBM: **c**, **f**, **i**) in CASE2.

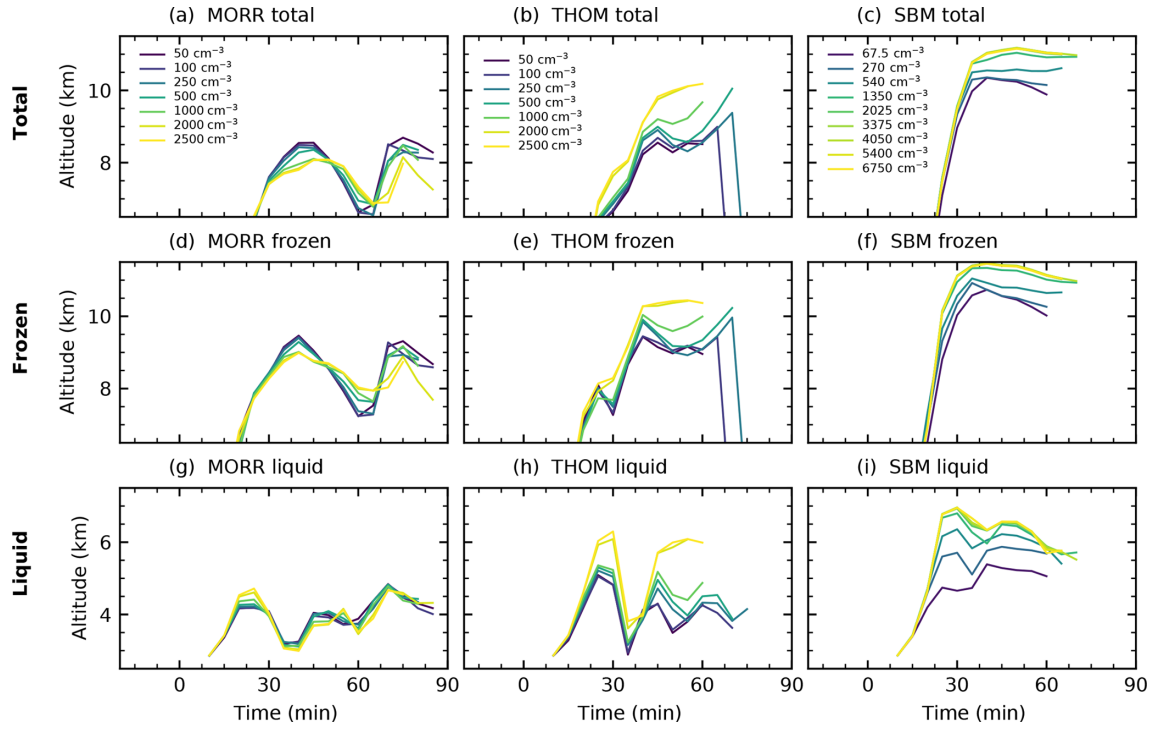

Figure 16. Altitude of the centre of gravity of the cloud and the individual phases in the analysed left-moving cell for the three different microphysics schemes (Morrison: **a**, **d**, **g**, Thompson: **b**, **e**, **h**, SBM: **c**, **f**, **i**) in CASE2.

only about 30 % smaller than in CASE1 (Fig. 15a, b, c), which includes much more frozen hydrometeor mass than the two bulk microphysics schemes (Fig. 15d, e, f), while liquid-phase mass is similar between the three microphysics schemes (Fig. 15g, h, i).

The effects of a variation of CDNC are quite similar to the ones seen in CASE1 for the two bulk microphysics schemes (Fig. 15a, b). The simulations with the Morrison scheme show a relatively small decrease in cloud mass, while cloud mass increased by about 15 % for the Thompson microphysics scheme. These changes are almost entirely due to changes in the ice phase of the clouds with insignificant effects of a variation in the liquid phase (Fig. 15g, h) for both bulk schemes. The simulations with the spectral-bin microphysics scheme, however, show an opposite response compared to CASE1, with an increase in cloud mass of a similar magnitude to the variation in the two bulk microphysics schemes (Fig. 15c), which is dominated by changes in the ice phase (Fig. 15f). There is a significant increase of almost 50 % in cloud liquid mass in the earlier stages of the cloud evolution (Fig. 15i) at around 25 min of simulation time between the cleanest and the most polluted simulations with the SBM scheme. This coincides with a delayed evolution of the ice phase during that period of the developing cloud.

The changes in the altitude of the centre of gravity show less clear relationships with changes in the aerosol proxies CDNC/CCN in this case for the two bulk microphysics schemes. The Morrison scheme (Fig. 16a, d, g) has the strongest variation in the time evolution of the altitude of the centre of gravity, but generally shows a decrease in the altitude for both the liquid and ice phases in the cloud. In the Thompson scheme (Fig. 16b, e, h) increased CDNC leads to an increase in the height of the centre of gravity of the entire cloud and of both phases of water in the cloud. Similarly, increasing CCN in the spectral-bin microphysics scheme (Fig. 16c, f, i) leads to a strong increase in the altitude of the cloud mass and the individual phases, with the COG of total mass about 1.5 km higher in the most polluted case (6750 cm^{-3}) compared to the clean case (67.5 cm^{-3}) and an even stronger shift of up to 2 km in the liquid phase. All the SBM simulations with a higher CCN value than about 1500 cm^{-3} lead to relatively similar results, which means that the aerosol effects saturate at this value.

4 Conclusions

We investigated the effects of changes in cloud droplet number concentration (CDNC) and cloud condensation nuclei (CCN) concentrations on the development of idealised simulations of deep convection to test proposed aerosol effects. This includes different mechanisms of convective invigoration (Rosenfeld et al., 2008; Lebo and Seinfeld, 2011; Fan et al., 2013; Grabowski and Morrison, 2016). A combination of cell tracking and detailed process-rate diagnostics was

used to investigate the evolution and structure of the microphysical processes in individual deep convective cells. We used three different cloud microphysics schemes (two bulk schemes and one bin scheme) to investigate how the choice of microphysics scheme affects these results. By covering a wide range of values of CDNC/CCN representative of conditions from very clean to very polluted, we were able to look for consistent responses of the clouds to changes in these aerosol proxies and thus go beyond a simple comparison of just clean and polluted conditions.

An increase in cloud droplet number concentration from values representing clean conditions ($\mathrm{CDNC} = 50\,\mathrm{cm}^{-3}$) to strongly polluted conditions ($\mathrm{CDNC} = 2500\,\mathrm{cm}^{-3}$) leads to a shift of freezing processes to higher levels in both bulk microphysics schemes. Detailed analyses of the individual process rates confirmed that this is indeed related to a shift from freezing of rain to freezing of cloud droplets and a decrease in riming of raindrops due to larger amounts of liquid water in the form of cloud droplets instead of rain. This, in turn, can be related to the changes in autoconversion and accretion in the warm-phase region of the cloud. This is in line with the first step of the mechanisms proposed for convective invigoration of deep convection due to an increase in aerosols acting as CCN (e.g. Rosenfeld et al., 2008; Lebo and Seinfeld, 2011; Fan et al., 2013; Altaratz et al., 2014). These changes are concurrent and linked to changes in the prevailing hydrometeors in the different parts of the clouds. Both bulk microphysics schemes showed a strong increase in cloud droplet mass mixing ratio at the expense of raindrops for increased CDNC. This shift leads to a significant increase in the height of freezing and riming processes, which shifts the latent heat release from freezing upwards by about 2 km. This response is consistent between the different microphysics schemes and confirms earlier studies that stated the importance of changes in the partition between rain and cloud droplets in determining the evolution of freezing and riming (Seifert and Beheng, 2006; Kalina et al., 2014). The simulations with the SBM scheme show an upward shift in latent heating that is very similar to the one observed for the two bulk schemes and associated with the lifting of the freezing and riming processes. This confirms that the effect is not just an artefact of the separate treatment of raindrops and cloud droplets in the bulk microphysics schemes or the application of saturation adjustment. In the ice phase of the clouds, there is a clear shift from mainly graupel or hail in the low-CDNC simulations to larger fractions of snow and ice crystals in the high-CDNC simulation.

A more detailed analysis of the different components of the latent heating for the two bulk microphysics schemes shows a complex superposition of changes to the different phase changes in the tracked cells. This confirms results from previous studies on the effects of aerosols on supercells (Khain et al., 2008; Morrison, 2012; Kalina et al., 2014) and other deep convective clouds (Ekman et al., 2011) that pointed out a range of compensating processes limiting convective invigoration and a strong dependency on the environmental conditions in which the cloud develops. Condensation and evaporation are the largest contributions to latent heating and cooling in the cloud. The relative changes in these two processes due to changes in the aerosol proxies are comparatively small, except for the changes in the evaporation of rain due to the strong decrease in the formation of rain. This is to be expected, as condensation and evaporation of cloud droplets in the two bulk microphysics schemes are represented using saturation adjustment, which does not include the effect of changes in cloud drop radius on the condensation and evaporation processes. Saturation adjustment has the potential to mask the effects of aerosols in highly supersaturated strong convective updrafts as described, e.g. in Lebo et al. (2012) and Fan et al. (2018). Lebo et al. (2012) argue that saturation adjustment, as used in both bulk microphysics schemes in this study, leads to an artificial increase in condensation in the lower levels of the clouds, which would limit the effects of aerosol concentrations on buoyancy in mid and high levels.

There are significant differences between the two bulk schemes in the profiles of sublimation and deposition as well as in the response of these processes to changes in CDNC. This can be attributed to different parameter choices in the schemes. The strongest differences result from the fact that deposition onto graupel hydrometeors is not allowed to occur in the Thompson microphysics scheme, which leads to a strong increase in deposition due to the replacement of graupel by the other ice-phase hydrometeors on which deposition occurs. This strong increase in deposition additionally drives changes in condensation and evaporation in the mixed-phase region of the cloud via the Wegener–Bergeron–Findeisen process. By effectively removing water vapour, this leads to a noticeable feedback on the evaporation and condensation on cloud droplets that are intrinsically not affected by changes in CDNC because of the use of saturation adjustment. It was also shown that the melting of frozen hydrometeors contributes significantly to the formation of raindrops, especially under high CDNC conditions, which forms an additional important feedback of changes in the ice-phase onto the warm-phase processes.

The changes to the individual components of integrated latent heating in the cloud due to a variation of CDNC compensate each other in the two bulk microphysics schemes. Hence, there is no significant change in the total integrated latent heating in the cloud with changes in CDNC/CCN and no thermodynamic invigoration from changes in the microphysics due to the change in the aerosol proxies. This result is confirmed in the SBM simulations, that also do not show any significant change in vertically integrated latent heating for a variation of CCN. Therefore, the absence of convective invigoration in the bulk microphysics schemes cannot be solely attributed to the application of saturation adjustment.

The analysis of the clouds with respect to the total cloud mass and the altitude of the centre of gravity showed

some contrasting results between the different microphysics schemes. There is a clear signal of a lifting of all parts of the clouds to higher altitude under polluted conditions, probably associated with the changes in the ice-phase hydrometeor partition. This agrees with findings from, e.g. Fan et al. (2013), reporting substantial changes to cloud height and even in the absence of convective invigoration in the form of increased total latent heating in the cloud. However, the analysis of cloud mass revealed opposing trends in the response between the three microphysics schemes. There is no clear pattern in the different responses to CDNC/CCN with regard to these bulk cloud properties, with variations between the two bulk microphysics schemes often as large as between the bulk schemes and the spectral-bin microphysics scheme, which confirms the strong differences between microphysics schemes found in previous studies (Lebo et al., 2012; Khain et al., 2015; White et al., 2017).

The results for the first case (CASE1), based on Weisman and Klemp (1982), are supported by the analysis of a second idealised supercell case (CASE2), based on Kumjian et al. (2010) and Dawson et al. (2013). The microphysical process-rate diagnostics revealed similar changes in rain formation and the altitude of freezing and riming processes for the two bulk microphysics schemes in this second case. All three microphysics schemes showed that the effects of a variation of CDNC or CCN saturate above a threshold value in both simulated cases. Variations above a CDNC of around $2000\,\mathrm{cm}^{-3}$ in the bulk schemes and above a CCN concentration of $1500\,\mathrm{cm}^{-3}$ in the bin microphysics scheme do not lead to any further changes in the convective clouds with regard to cloud condensate mass or altitude. This confirms results from previous studies such as Kalina et al. (2014) that reported a saturation of aerosol effects at similar values.

The pathway analysis developed for this study also includes the process rates for the number concentrations of the different hydrometeors. This includes processes like ice multiplication that could play an important role in better understanding some of the possible pathways of aerosol effects on convective clouds (Fan et al., 2013, 2016).

This work focused on the analysis of microphysical pathways of aerosol effects on deep convective clouds in an idealised framework. To test the robustness of the results under realistic scenarios, including potential buffering mechanisms, we are currently applying our analysis framework to large case study simulations of isolated convection over the area around Houston, Texas, as part of the ACPC initiative (Aerosol, Cloud, Precipitation, and Climate Working Group, http://www.acpcinitiative.org, last access: 24 February 2019). We apply the cell tracking algorithm and the analysis of the detailed process-rate output developed in this study for a range of different cloud-resolving models and contrasting aerosol conditions. In these simulations, the individual deep convective clouds in the cloud field evolve and interact freely, which allows for a thorough analysis of important aspects such as the impact of aerosol conditions on the cell lifetimes or the statistics of the cloud size spectrum. The introduction of parameters describing the entire convective cell such as cloud mass and the position of the centre of gravity can contribute to a meaningful analysis of cloud field simulations with a large number of individual clouds.

The understanding of the detailed structure of microphysical processes in individually tracked deep convective clouds and the analysis of the pathways through which aerosol perturbations affect the deep convective clouds advance our understanding of aerosol–cloud interactions. This can be used to inform the parameterisation of microphysical processes and aerosol–convection interactions in global climate models. Recent developments in the use of global cloud-resolving models in climate research (e.g. Ban et al., 2014; Seiki et al., 2014; Sato et al., 2018) further motivate a detailed understanding of the pathways of aerosol effects on convective clouds and the uncertainties in their representation in numerical models.

Code availability. The WRF model is publicly available at http://www2.mmm.ucar.edu/wrf/users/ (WRF Community, 2000, last access: 24 February 2019). The code of the modified WRF model with the microphysical pathway diagnostics for the two bulk microphysics schemes and the additional second supercell case is available from the authors on request along with postprocessing code for the process rate analysis in Python. The tracking algorithm applied in this study has been developed into the tracking framework tobac (Tracking and Object-Based Analysis of Clouds) hosted on GitHub at https://github.com/climate-processes/tobac (last access: 24 February 2019). The version of the code used in this paper is available at https://doi.org/10.5281/zenodo.2577047 (Heikenfeld, 2019). The tracking makes use of the trackpy library (Allan et al., 2016).

Appendix A: Convective cell tracking and cell-based analysis

The tracking algorithm tracks individual convective cells and their volume based on the model output fields of vertical velocity and total condensate mixing ratio. The tracking of maxima in the column vertical velocity field is performed using trackpy (Allan et al., 2016). The algorithm from trackpy that is used to identify the updraft features requires an initial assumption for the size of the tracked object. We chose a diameter of 15 km to represent the large convective updrafts in the supercell cases. Tracked updrafts are required to exist for six output time steps, i.e. 30 min, to be included in the analysis, which helps to exclude spurious features in vertical velocity and thus focus on the analysis of properly developed deep convective cells. We extrapolate by two time steps at the beginning and at the end of each tracked trajectory to include a representation of the initial development of the convective clouds and the evolution after the weakening of the central updraft.

The volume of the convective clouds is determined by a watershedding algorithm using a fixed threshold to determine the extent of the individual clouds based on the tracked updrafts. We use a threshold of 1 $\mathrm{g\,cm^{-3}}$ for the total water content in this study, and a variation of this threshold by an order of magnitude to 0.1 $\mathrm{g\,cm^{-3}}$ showed that choosing a lower threshold did not significantly change the cloud volume and cloud mass or any of the more detailed process analyses.

Appendix B: Microphysics schemes and process-rate diagnostics

Tables B1 and B2 give an overview of the microphysical process rates for the hydrometeor masses as they are implemented in the two bulk microphysics schemes (Thompson et al., 2008; Morrison et al., 2009) studied in this paper.

In the Thompson scheme, some of the process rates are defined as signed variables representing two opposed processes. In these cases, we have used the process-rate variable with the positive sign for the respective process and ignored the values with the negative sign, which are covered by the opposing process (e.g. PRG_RCG for riming of rain on graupel and PRR_RCG for melting of graupel due to the collection by rain). Condensation/evaporation processes and deposition/sublimation processes are only defined through one combined process rate variable in the code. We have thus added the process rates with a negative sign as a variable in our diagnostics (e.g. E_PRW_VCD for the evaporation of droplets in addition to PRW_VCD for condensation) to allow for independent analyses of these, e.g. when aggregating the variables in space or time.

Ice multiplication according to the Hallet–Mossop process is implemented differently in the two bulk microphysics schemes. In the Morrison scheme, this is implemented as a direct transfer of water mass from the liquid phase to ice particles and considered to be contributing to riming. In the Thompson scheme, however, it forms a transfer from the frozen hydrometeor to new ice particles and is thus part of the "ice processes". Hence, these processes are found in different categories in the two tables presenting the process rates. As the actual mass transfer is negligibly small, this difference between the schemes is not relevant for the analyses performed in this study.

In the Morrison microphysics scheme as used in this study, the autoconversion of cloud droplets and accretion by rain are parameterised based on Khairoutdinov and Kogan (2000) and ice nucleation is based on Cooper (1986) and Rasmussen et al. (2002). The Thompson scheme applies an autoconversion parameterisation based on Berry and Reinhardt (1974), while the different freezing modes follow Bigg (1953), Cooper (1986) and Koop et al. (2000).

The two bulk microphysics schemes differ in important parameters regarding the different hydrometeor classes. The Morrison microphysics scheme is used in its configuration that treats the dense frozen hydrometeors as hail with a density of 900 $\mathrm{kg\,m^{-3}}$, while the simulations with the Thompson microphysics used graupel with a density of 500 $\mathrm{kg\,m^{-3}}$. The density of cloud ice, however, is higher in the simulations with the Thompson scheme 890 $\mathrm{kg\,m^{-3}}$ compared to the Morrison scheme (500 $\mathrm{kg\,m^{-3}}$), while snow density is set to 100 $\mathrm{kg\,m^{-3}}$ for both schemes. The Thompson scheme has a more complex treatment of the snow hydrometeor class compared to the Morrison scheme, making use of a combination of two size distributions and thus allowing for a variation of the density over its evolution (Field et al., 2005; Thompson et al., 2008). The fall speed calculations are based on different equations in the two microphysics schemes, all parameters for the hydrometeor classes are left at their default values.

Table B1. Mass transfer process rates for the Morrison microphysics scheme (Morrison et al., 2009).

Variable	Description	from	to	Grouping
PCC	Condensation on droplets	vapour	droplets	Condensation
EPCC	Evaporation of droplets	droplets	vapour	Evaporation
PRE	Evaporation of rain	rain	vapour	
PRC	Autoconversion	droplets	rain	Rain formation
PRA	Accretion	droplets	rain	
MNUCCC	Contact freezing of droplets	droplets	ice	Freezing
MNUCCD	Primary ice nucleation	droplets	ice	
QICF	Homogeneous freezing of droplets	droplets	ice	
MNUCCR	Contact freezing of rain	rain	ice	
QGRF	Homogeneous freezing of rain	rain	graupel	
QNIRF	Homogeneous freezing of rain	rain	snow	
PSACWS	Riming on snow	droplets	snow	Riming
PSACWI	Riming on ice	droplets	ice	
PSACWG	Collection of droplets by graupel	droplets	graupel	
PGSACW	Collection of droplets by snow	droplets	graupel	
PRACS	Rain–snow collection	rain	snow	
PIACR	Ice–rain collision	rain	graupel	
PIACRS	Ice–rain collision	rain	snow	
PRACG	Collection of rain by graupel	rain	graupel	
PGRACS	Collection of rain by snow	rain	graupel	
QMULTG	Ice multiplication droplets and graupel	droplets	ice	
QMULTS	Ice multiplication droplets and snow	droplets	ice	
QMULTRG	Ice multiplication rain and graupel	rain	ice	
QMULTR	Ice multiplication rain and snow	rain	ice	
PGMLT	Melting of graupel	graupel	rain	Melting
QIIM	Melting of ice	ice	droplets	
PSMLT	Melting of snow	snow	rain	
PRD	Deposition on ice	vapour	ice	Deposition
PRDS	Deposition on snow	vapour	snow	
PRDG	Deposition on graupel	vapour	graupel	
EPRDG	Sublimation of graupel	graupel	vapour	Sublimation
EVPMG	Graupel melting and evaporating	graupel	vapour	
EPRD	Sublimation of ice	ice	vapour	
EPRDS	Sublimation of snow	snow	vapour	
EVPMS	Snow melting and evaporating	snow	vapour	
PRAI	Accretion of cloud ice by snow	ice	snow	Ice processes
PRCI	Autoconversion of cloud ice to snow	ice	snow	
PRACI	Ice–rain collection (ice to graupel)	ice	graupel	
PRACIS	Ice–rain collision (ice to snow)	ice	snow	
PSACR	Collection of snow by rain	snow	graupel	

Table B2. Mass transfer process rates for the Thompson microphysics scheme (Thompson et al., 2008). * denotes processes that are implemented but disabled in the microphysics scheme.

Variable	Description	from	to	Grouping
PRW_VCD	Condensation	vapour	droplets	Condensation
PRV_REV	Evaporation of rain	vapour	droplets	Evaporation
E_PRW_VCD	Evaporation of cloud droplets	droplets	vapour	
PRR_WAU	Autoconversion	droplets	rain	Rain formation
PRR_RCW	Accretion	droplets	rain	
PRI_WFZ	Freezing of cloud droplets	droplets	ice	Freezing
PRI_RFZ	Freezing of rain to ice	rain	ice	
PRG_RFZ	Freezing of rain to graupel	rain	graupel	
PRS_SCW	Collection of droplets by snow	droplets	snow	Riming
PRG_SCW	Collection of droplets by snow	droplets	snow	
PRG_GCW	Collection of droplets by graupel	droplets	graupel	
PRG_RCG	Collection of rain by graupel	rain	graupel	
PRR_RCS	Collection of rain by snow	rain	snow	
PRR_RCS	Collection of rain by snow	rain	graupel	
PRR_RCI	Collection of ice by rain	rain	graupel	
PRW_IMI	Melting of ice	ice	rain	Melting
PRR_GML	Melting of graupel	graupel	rain	
PRR_RCS	Collection of snow by rain	snow	rain	
PRR_RCG	Collection of graupel by rain	graupel	rain	
PRS_SDE	Deposition on snow	vapour	snow	Deposition
PRS_IDE	Deposition on ice to snow	vapour	snow	
PRI_IDE	Deposition on ice	vapour	ice	
PRG_GDE*	Deposition on graupel	vapour	graupel	
PRI_INU	Ice nucleation	vapour	ice	
PRI_IHA*	Freezing of aqueous aerosols	vapour	ice	
E_PRS_SDE	Sublimation of snow	snow	vapour	Sublimation
E_PRI_IDE	Sublimation of ice	ice	vapour	
E_PRG_GDE	Sublimation of graupel	graupel	vapour	
PRS_SCI	Collection of ice by snow to graupel	ice	graupel	Ice processes
PRS_IHM	Hallet–Mossop process	snow	ice	
PRS_IAU	Autoconversion of ice to snow	ice	snow	
E_PRS_RCS	Collection of snow by rain	snow	graupel	
PRI_RCI	Collection of ice by rain	ice	graupel	
PRG_IHM	Hallet–Mossop process	graupel	ice	

Author contributions. MH, BW, LL and PS designed the experiment, MH and BW implemented the microphysical pathway analysis in WRF, MH set up the simulations and developed the data analysis including the tracking algorithm, MH wrote the manuscript and BW, PS and LL contributed to the analysis and the manuscript.

Competing interests. The authors declare that they have no conflict of interest.

Special issue statement. This article is part of the special issue "BACCHUS – Impact of Biogenic versus Anthropogenic emissions on Clouds and Climate: towards a Holistic UnderStanding (ACP/AMT/GMD inter-journal SI)". It is not associated with a conference.

Acknowledgements. Max Heikenfeld acknowledges funding from the NERC Oxford DTP in Environmental Research (NE/L002612/1). The research leading to these results has received funding from the European Union's Seventh Framework Programme (FP7/2007-2013) project BACCHUS under grant agreement no. 603445 (Max Heikenfeld, Philip Stier and Laurent Labbouz). The authors acknowledge funding from the European Research Council project ACCLAIM (Philip Stier and Bethan White) under grant agreement no. 28002 from the European Union's Seventh Framework Programme (FP7/2007-2013). Philip Stier and Max Heikenfeld acknowledge funding from the European Research Council project RECAP under the European Union's Horizon 2020 research and innovation programme with grant agreement 724602. Laurent Labbouz has also been supported by CNES. Bethan White has also received funding from the Australian Government through the Australian Research Council. The authors would like to acknowledge the use of the University of Oxford Advanced Research Computing (ARC) facility (https://doi.org/10.5281/zenodo.22558) in carrying out this work. We want to thank Hugh Morrison and Greg Thompson for important discussions about the two bulk microphysics schemes used in the study and Matthew Christensen for helpful comments on the manuscript.

Edited by: Leiming Zhang
Reviewed by: three anonymous referees

References

Allan, D., Caswell, T., Keim, N., and van der Wel, C.: Trackpy: Trackpy v0.3.2, Zenodo, https://doi.org/10.5281/zenodo.60550, 2016.

Altaratz, O., Koren, I., Remer, L. A., and Hirsch, E.: Review: Cloud Invigoration by Aerosols – Coupling between Microphysics and Dynamics, Atmos. Res., 140–141, 38–60, https://doi.org/10.1016/j.atmosres.2014.01.009, 2014.

Andreae, M. O., Rosenfeld, D., Artaxo, P., Costa, A. A., Frank, G. P., Longo, K. M., and Silva-Dias, M. A. F.: Smoking Rain Clouds over the Amazon, Science, 303, 1337–1342, https://doi.org/10.1126/science.1092779, 2004.

Ban, N., Schmidli, J., and Schär, C.: Evaluation of the Convection-Resolving Regional Climate Modeling Approach in Decade-Long Simulations, J. Geophys. Res.-Atmos., 119, 7889–7907, https://doi.org/10.1002/2014JD021478, 2014.

Berry, E. X. and Reinhardt, R. L.: An Analysis of Cloud Drop Growth by Collection Part II. Single Initial Distributions, J. Atmos. Sci., 31, 1825–1831, https://doi.org/10.1175/1520-0469(1974)031<1825:AAOCDG>2.0.CO;2, 1974.

Bigg, E. K.: The Supercooling of Water, P. Phys. Soc. Lond. B, 66, 688, https://doi.org/10.1088/0370-1301/66/8/309, 1953.

Boucher, O., Randall, D., Artaxo, P., Bretherton, C., Feingold, G., Forster, P., Kerminen, V.-M., Kondo, Y., Liao, H., Lohmann, U., Rasch, P., Satheesh, S., Sherwood, S., Stevens, B., and Zhang, X.: Clouds and Aerosols, in: Climate Change 2013: The Physical Science Basis. Contribution of Working Group I to the Fifth Assessment Report of the Intergovernmental Panel on Climate Change, edited by: Stocker, T., Qin, D., Plattner, G.-K., Tignor, M., Allen, S., Boschung, J., Nauels, A., Xia, Y., Bex, V., and Midgley, P., 571–658, Cambridge University Press, Cambridge, United Kingdom and New York, NY, USA, https://doi.org/10.1017/CBO9781107415324.016, 2013.

Chang, D., Cheng, Y., Reutter, P., Trentmann, J., Burrows, S. M., Spichtinger, P., Nordmann, S., Andreae, M. O., Pöschl, U., and Su, H.: Comprehensive mapping and characteristic regimes of aerosol effects on the formation and evolution of pyro-convective clouds, Atmos. Chem. Phys., 15, 10325–10348, https://doi.org/10.5194/acp-15-10325-2015, 2015.

Chen, Q., Koren, I., Altaratz, O., Heiblum, R. H., Dagan, G., and Pinto, L.: How do changes in warm-phase microphysics affect deep convective clouds?, Atmos. Chem. Phys., 17, 9585–9598, https://doi.org/10.5194/acp-17-9585-2017, 2017.

Cooper, W. A.: Ice Initiation in Natural Clouds, in: Precipitation Enhancement – A Scientific Challenge, Meteorological Monographs, 29–32, American Meteorological Society, Boston, MA, https://doi.org/10.1007/978-1-935704-17-1_4, 1986.

Dagan, G., Koren, I., and Altaratz, O.: Aerosol Effects on the Timing of Warm Rain Processes, Geophys. Res. Lett., 42, 4590–4598, https://doi.org/10.1002/2015GL063839, 2015.

Dagan, G., Koren, I., Altaratz, O., and Heiblum, R. H.: Time-dependent, non-monotonic response of warm convective cloud fields to changes in aerosol loading, Atmos. Chem. Phys., 17, 7435–7444, https://doi.org/10.5194/acp-17-7435-2017, 2017.

Dagan, G., Koren, I., and Altaratz, O.: Quantifying the effect of aerosol on vertical velocity and effective terminal velocity in warm convective clouds, Atmos. Chem. Phys., 18, 6761–6769, https://doi.org/10.5194/acp-18-6761-2018, 2018.

Dawe, J. T. and Austin, P. H.: Statistical analysis of an LES shallow cumulus cloud ensemble using a cloud tracking algorithm, Atmos. Chem. Phys., 12, 1101–1119, https://doi.org/10.5194/acp-12-1101-2012, 2012.

Dawson, D. T., Mansell, E. R., Jung, Y., Wicker, L. J., Kumjian, M. R., and Xue, M.: Low-Level ZDR Signatures in Supercell Forward Flanks: The Role of Size Sorting and Melting of Hail, J. Atmos. Sci., 71, 276–299, https://doi.org/10.1175/JAS-D-13-0118.1, 2013.

Ekman, A. M. L., Engström, A., and Söderberg, A.: Impact of Two-Way Aerosol–Cloud Interaction and Changes in Aerosol Size Distribution on Simulated Aerosol-Induced Deep

Convective Cloud Sensitivity, J. Atmos. Sci., 68, 685–698, https://doi.org/10.1175/2010JAS3651.1, 2011.

Emanuel, K. A.: Atmospheric Convection, Oxford University Press, New York, 1994.

Fan, J., Rosenfeld, D., Ding, Y., Leung, L. R., and Li, Z.: Potential Aerosol Indirect Effects on Atmospheric Circulation and Radiative Forcing through Deep Convection, Geophys. Res. Lett., 39, L09806, https://doi.org/10.1029/2012GL051851, 2012.

Fan, J., Leung, L. R., Rosenfeld, D., Chen, Q., Li, Z., Zhang, J., and Yan, H.: Microphysical Effects Determine Macrophysical Response for Aerosol Impacts on Deep Convective Clouds, P. Natl. Acad. Sci. USA, 110, E4581–E4590, https://doi.org/10.1073/pnas.1316830110, 2013.

Fan, J., Wang, Y., Rosenfeld, D., and Liu, X.: Review of Aerosol–Cloud Interactions: Mechanisms, Significance, and Challenges, J. Atmos. Sci., 73, 4221–4252, https://doi.org/10.1175/JAS-D-16-0037.1, 2016.

Fan, J., Rosenfeld, D., Zhang, Y., Giangrande, S. E., Li, Z., Machado, L. A. T., Martin, S. T., Yang, Y., Wang, J., Artaxo, P., Barbosa, H. M. J., Braga, R. C., Comstock, J. M., Feng, Z., Gao, W., Gomes, H. B., Mei, F., Pöhlker, C., Pöhlker, M. L., Pöschl, U., and de Souza, R. A. F.: Substantial Convection and Precipitation Enhancements by Ultrafine Aerosol Particles, Science, 359, 411–418, https://doi.org/10.1126/science.aan8461, 2018.

Field, P. R., Hogan, R. J., Brown, P. R. A., Illingworth, A. J., Choularton, T. W., and Cotton, R. J.: Parametrization of Ice-Particle Size Distributions for Mid-Latitude Stratiform Cloud, Q. J. Roy. Meteor. Soc., 131, 1997–2017, https://doi.org/10.1256/qj.04.134, 2005.

Findeisen, W.: Kolloid-Meteorologische Vorgänge Bei Niederschlags-Bildung, Meteorol. Z., 55, 121–133, 1938.

Findeisen, W., Volken, E., Giesche, A. M., and Brönnimann, S.: Colloidal Meteorological Processes in the Formation of Precipitation, Meteorol. Z., 24, 443–454, 2015.

Gettelman, A.: Putting the clouds back in aerosol–cloud interactions, Atmos. Chem. Phys., 15, 12397–12411, https://doi.org/10.5194/acp-15-12397-2015, 2015.

Ghan, S. J., Abdul-Razzak, H., Nenes, A., Ming, Y., Liu, X., Ovchinnikov, M., Shipway, B., Meskhidze, N., Xu, J., and Shi, X.: Droplet Nucleation: Physically-Based Parameterizations and Comparative Evaluation, J. Adv. Model. Earth Sy., 3, M10001, https://doi.org/10.1029/2011MS000074, 2011.

Glassmeier, F. and Lohmann, U.: Constraining Precipitation Susceptibility of Warm-, Ice-, and Mixed-Phase Clouds with Microphysical Equations, J. Atmos. Sci., 73, 5003–5023, https://doi.org/10.1175/JAS-D-16-0008.1, 2016.

Grabowski, W. W. and Morrison, H.: Untangling Microphysical Impacts on Deep Convection Applying a Novel Modeling Methodology. Part II: Double-Moment Microphysics, J. Atmos. Sci., 73, 3749–3770, https://doi.org/10.1175/JAS-D-15-0367.1, 2016.

Guo, H., Golaz, J.-C., Donner, L. J., Wyman, B., Zhao, M., and Ginoux, P.: CLUBB as a Unified Cloud Parameterization: Opportunities and Challenges, Geophys. Res. Lett., 42, 4540–4547, https://doi.org/10.1002/2015GL063672, 2015.

Harrington, J. Y., Sulia, K., and Morrison, H.: A Method for Adaptive Habit Prediction in Bulk Microphysical Models. Part I: Theoretical Development, J. Atmos. Sci., 70, 349–364, https://doi.org/10.1175/JAS-D-12-040.1, 2013a.

Harrington, J. Y., Sulia, K., and Morrison, H.: A Method for Adaptive Habit Prediction in Bulk Microphysical Models. Part II: Parcel Model Corroboration, J. Atmos. Sci., 70, 365–376, https://doi.org/10.1175/JAS-D-12-0152.1, 2013b.

Heiblum, R. H., Altaratz, O., Koren, I., Feingold, G., Kostinski, A. B., Khain, A. P., Ovchinnikov, M., Fredj, E., Dagan, G., Pinto, L., Yaish, R., and Chen, Q.: Characterization of Cumulus Cloud Fields Using Trajectories in the Center of Gravity versus Water Mass Phase Space: 2. Aerosol Effects on Warm Convective Clouds, J. Geophys. Res.-Atmos., 121, 2015JD024193, https://doi.org/10.1002/2015JD024193, 2016a.

Heiblum, R. H., Altaratz, O., Koren, I., Feingold, G., Kostinski, A. B., Khain, A. P., Ovchinnikov, M., Fredj, E., Dagan, G., Pinto, L., Yaish, R., and Chen, Q.: Characterization of Cumulus Cloud Fields Using Trajectories in the Center of Gravity versus Water Mass Phase Space: 1. Cloud Tracking and Phase Space Description, J. Geophys. Res.-Atmos., 121, 2015JD024186, https://doi.org/10.1002/2015JD024186, 2016b.

Heikenfeld, M.: tobac 0.6.9: Tracking and Object-Based Analysis of Clouds, Zenodo, https://doi.org/10.5281/zenodo.2577047, 2019.

Heus, T. and Seifert, A.: Automated tracking of shallow cumulus clouds in large domain, long duration large eddy simulations, Geosci. Model Dev., 6, 1261–1273, https://doi.org/10.5194/gmd-6-1261-2013, 2013.

Igel, A. L., Igel, M. R., and van den Heever, S. C.: Make It a Double? Sobering Results from Simulations Using Single-Moment Microphysics Schemes, J. Atmos. Sci., 72, 910–925, https://doi.org/10.1175/JAS-D-14-0107.1, 2014.

Kalina, E. A., Friedrich, K., Morrison, H., and Bryan, G. H.: Aerosol Effects on Idealized Supercell Thunderstorms in Different Environments, J. Atmos. Sci., 71, 4558–4580, https://doi.org/10.1175/JAS-D-14-0037.1, 2014.

Khain, A. and Lynn, B.: Simulation of a Supercell Storm in Clean and Dirty Atmosphere Using Weather Research and Forecast Model with Spectral Bin Microphysics, J. Geophys. Res.-Atmos., 114, D19209, https://doi.org/10.1029/2009JD011827, 2009.

Khain, A., Pokrovsky, A., Pinsky, M., Seifert, A., and Phillips, V.: Simulation of Effects of Atmospheric Aerosols on Deep Turbulent Convective Clouds Using a Spectral Microphysics Mixed-Phase Cumulus Cloud Model. Part I: Model Description and Possible Applications, J. Atmos. Sci., 61, 2963–2982, https://doi.org/10.1175/JAS-3350.1, 2004.

Khain, A. P., BenMoshe, N., and Pokrovsky, A.: Factors Determining the Impact of Aerosols on Surface Precipitation from Clouds: An Attempt at Classification, J. Atmos. Sci., 65, 1721–1748, https://doi.org/10.1175/2007JAS2515.1, 2008.

Khain, A. P., Phillips, V., Benmoshe, N., and Pokrovsky, A.: The Role of Small Soluble Aerosols in the Microphysics of Deep Maritime Clouds, J. Atmos. Sci., 69, 2787–2807, https://doi.org/10.1175/2011JAS3649.1, 2012.

Khain, A. P., Beheng, K. D., Heymsfield, A., Korolev, A., Krichak, S. O., Levin, Z., Pinsky, M., Phillips, V., Prabhakaran, T., Teller, A., van den Heever, S. C., and Yano, J.-I.: Representation of Microphysical Processes in Cloud-Resolving Models: Spectral (Bin) Microphysics versus Bulk Parameterization, Rev. Geophys., 53, 247–322, https://doi.org/10.1002/2014RG000468, 2015.

Khairoutdinov, M. and Kogan, Y.: A New Cloud Physics Parameterization in a Large-Eddy Simulation Model of Marine Stratocumulus, Mon. Weather Rev., 128, 229–243, https://doi.org/10.1175/1520-0493(2000)128<0229:ANCPPI>2.0.CO;2, 2000.

Kipling, Z., Stier, P., Labbouz, L., and Wagner, T.: Dynamic subgrid heterogeneity of convective cloud in a global model: description and evaluation of the Convective Cloud Field Model (CCFM) in ECHAM6–HAM2, Atmos. Chem. Phys., 17, 327–342, https://doi.org/10.5194/acp-17-327-2017, 2017.

Koop, T., Luo, B., Tsias, A., and Peter, T.: Water Activity as the Determinant for Homogeneous Ice Nucleation in Aqueous Solutions, Nature, 406, 611–614, https://doi.org/10.1038/35020537, 2000.

Koren, I., Altaratz, O., Feingold, G., Levin, Z., and Reisin, T.: Cloud's Center of Gravity – a compact approach to analyze convective cloud development, Atmos. Chem. Phys., 9, 155–161, https://doi.org/10.5194/acp-9-155-2009, 2009.

Koren, I., Remer, L. A., Altaratz, O., Martins, J. V., and Davidi, A.: Aerosol-induced changes of convective cloud anvils produce strong climate warming, Atmos. Chem. Phys., 10, 5001–5010, https://doi.org/10.5194/acp-10-5001-2010, 2010.

Kumjian, M. R., Ryzhkov, A. V., Melnikov, V. M., and Schuur, T. J.: Rapid-Scan Super-Resolution Observations of a Cyclic Supercell with a Dual-Polarization WSR-88D, Mon. Weather Rev., 138, 3762–3786, https://doi.org/10.1175/2010MWR3322.1, 2010.

Labbouz, L., Kipling, Z., Stier, P., and Protat, A.: How Well Can We Represent the Spectrum of Convective Clouds in a Climate Model? Comparisons between Internal Parameterization Variables and Radar Observations, J. Atmos. Sci., 75, 1509–1524, https://doi.org/10.1175/JAS-D-17-0191.1, 2018.

Lebo, Z. J. and Seinfeld, J. H.: Theoretical basis for convective invigoration due to increased aerosol concentration, Atmos. Chem. Phys., 11, 5407–5429, https://doi.org/10.5194/acp-11-5407-2011, 2011.

Lebo, Z. J., Morrison, H., and Seinfeld, J. H.: Are simulated aerosol-induced effects on deep convective clouds strongly dependent on saturation adjustment?, Atmos. Chem. Phys., 12, 9941–9964, https://doi.org/10.5194/acp-12-9941-2012, 2012.

Lohmann, U. and Feichter, J.: Global indirect aerosol effects: a review, Atmos. Chem. Phys., 5, 715–737, https://doi.org/10.5194/acp-5-715-2005, 2005.

Lynn, B. H., Khain, A. P., Dudhia, J., Rosenfeld, D., Pokrovsky, A., and Seifert, A.: Spectral (Bin) Microphysics Coupled with a Mesoscale Model (MM5). Part I: Model Description and First Results, Mon. Weather Rev., 133, 44–58, https://doi.org/10.1175/MWR-2840.1, 2005a.

Lynn, B. H., Khain, A. P., Dudhia, J., Rosenfeld, D., Pokrovsky, A., and Seifert, A.: Spectral (Bin) Microphysics Coupled with a Mesoscale Model (MM5). Part II: Simulation of a CaPE Rain Event with a Squall Line, Mon. Weather Rev., 133, 59–71, https://doi.org/10.1175/MWR-2841.1, 2005b.

Malavelle, F. F., Haywood, J. M., Jones, A., Gettelman, A., Clarisse, L., Bauduin, S., Allan, R. P., Karset, I. H. H., Kristjánsson, J. E., Oreopoulos, L., Cho, N., Lee, D., Bellouin, N., Boucher, O., Grosvenor, D. P., Carslaw, K. S., Dhomse, S., Mann, G. W., Schmidt, A., Coe, H., Hartley, M. E., Dalvi, M., Hill, A. A., Johnson, B. T., Johnson, C. E., Knight, J. R., O'Connor, F. M., Partridge, D. G., Stier, P., Myhre, G., Platnick, S., Stephens, G. L., Takahashi, H., and Thordarson, T.: Strong Constraints on Aerosol–Cloud Interactions from Volcanic Eruptions, Nature, 546, 485–491, https://doi.org/10.1038/nature22974, 2017.

Morrison, H.: On the robustness of aerosol effects on an idealized supercell storm simulated with a cloud system-resolving model, Atmos. Chem. Phys., 12, 7689–7705, https://doi.org/10.5194/acp-12-7689-2012, 2012.

Morrison, H. and Milbrandt, J.: Comparison of Two-Moment Bulk Microphysics Schemes in Idealized Supercell Thunderstorm Simulations, Mon. Weather Rev., 139, 1103–1130, https://doi.org/10.1175/2010MWR3433.1, 2010.

Morrison, H. and Milbrandt, J. A.: Parameterization of Cloud Microphysics Based on the Prediction of Bulk Ice Particle Properties. Part I: Scheme Description and Idealized Tests, J. Atmos. Sci., 72, 287–311, https://doi.org/10.1175/JAS-D-14-0065.1, 2014.

Morrison, H., Curry, J. A., and Khvorostyanov, V. I.: A New Double-Moment Microphysics Parameterization for Application in Cloud and Climate Models. Part I: Description, J. Atmos. Sci., 62, 1665–1677, https://doi.org/10.1175/JAS3446.1, 2005.

Morrison, H., Thompson, G., and Tatarskii, V.: Impact of Cloud Microphysics on the Development of Trailing Stratiform Precipitation in a Simulated Squall Line: Comparison of One- and Two-Moment Schemes, Mon. Weather Rev., 137, 991–1007, https://doi.org/10.1175/2008MWR2556.1, 2009.

Morrison, H., Milbrandt, J. A., Bryan, G. H., Ikeda, K., Tessendorf, S. A., and Thompson, G.: Parameterization of Cloud Microphysics Based on the Prediction of Bulk Ice Particle Properties. Part II: Case Study Comparisons with Observations and Other Schemes, J. Atmos. Sci., 72, 312–339, https://doi.org/10.1175/JAS-D-14-0066.1, 2015.

Naylor, J. and Gilmore, M. S.: Convective Initiation in an Idealized Cloud Model Using an Updraft Nudging Technique, Mon. Weather Rev., 140, 3699–3705, https://doi.org/10.1175/MWR-D-12-00163.1, 2012.

Nishant, N. and Sherwood, S. C.: A Cloud-Resolving Model Study of Aerosol-Cloud Correlation in a Pristine Maritime Environment, Geophys. Res. Lett., 44, 5774–5781, https://doi.org/10.1002/2017GL073267, 2017.

Rasmussen, R. M., Geresdi, I., Thompson, G., Manning, K., and Karplus, E.: Freezing Drizzle Formation in Stably Stratified Layer Clouds: The Role of Radiative Cooling of Cloud Droplets, Cloud Condensation Nuclei, and Ice Initiation, J. Atmos. Sci., 59, 837–860, https://doi.org/10.1175/1520-0469(2002)059<0837:FDFISS>2.0.CO;2, 2002.

Rosenfeld, D., Lohmann, U., Raga, G. B., O'Dowd, C. D., Kulmala, M., Fuzzi, S., Reissell, A., and Andreae, M. O.: Flood or Drought: How Do Aerosols Affect Precipitation?, Science, 321, 1309–1313, https://doi.org/10.1126/science.1160606, 2008.

Rosenfeld, D., Sherwood, S., Wood, R., and Donner, L.: Climate Effects of Aerosol-Cloud Interactions, Science, 343, 379–380, https://doi.org/10.1126/science.1247490, 2014.

Rothenberg, D., Avramov, A., and Wang, C.: On the representation of aerosol activation and its influence on model-derived estimates of the aerosol indirect effect, Atmos. Chem. Phys., 18, 7961–7983, https://doi.org/10.5194/acp-18-7961-2018, 2018.

Sato, Y., Goto, D., Michibata, T., Suzuki, K., Takemura, T., Tomita, H., and Nakajima, T.: Aerosol Effects on Cloud Water Amounts Were Successfully Simulated by a Global

Cloud-System Resolving Model, Nat. Commun., 9, 985, https://doi.org/10.1038/s41467-018-03379-6, 2018.

Schutgens, N. A. J. and Stier, P.: A pathway analysis of global aerosol processes, Atmos. Chem. Phys., 14, 11657–11686, https://doi.org/10.5194/acp-14-11657-2014, 2014.

Seifert, A. and Beheng, K. D.: A Two-Moment Cloud Microphysics Parameterization for Mixed-Phase Clouds. Part 2: Maritime vs. Continental Deep Convective Storms, Meteorol. Atmos. Phys., 92, 67–82, https://doi.org/10.1007/s00703-005-0113-3, 2006.

Seiki, T., Kodama, C., Noda, A. T., and Satoh, M.: Improvement in Global Cloud-System-Resolving Simulations by Using a Double-Moment Bulk Cloud Microphysics Scheme, J. Climate, 28, 2405–2419, https://doi.org/10.1175/JCLI-D-14-00241.1, 2014.

Simpson, E., Connolly, P., and McFiggans, G.: An investigation into the performance of four cloud droplet activation parameterisations, Geosci. Model Dev., 7, 1535–1542, https://doi.org/10.5194/gmd-7-1535-2014, 2014.

Skamarock, C., Klemp, B., Dudhia, J., Gill, O., Barker, D., Duda, G., Huang, X.-Y., Wang, W., and Powers, G.: A Description of the Advanced Research WRF Version 3, Tech. rep., https://doi.org/10.5065/D68S4MVH, 2008.

Song, X. and Zhang, G. J.: Microphysics Parameterization for Convective Clouds in a Global Climate Model: Description and Single-Column Model Tests, J. Geophys. Res.-Atmos., 116, D02201, https://doi.org/10.1029/2010JD014833, 2011.

Stevens, B. and Feingold, G.: Untangling Aerosol Effects on Clouds and Precipitation in a Buffered System, Nature, 461, 607–613, https://doi.org/10.1038/nature08281, 2009.

Storelvmo, T. and Tan, I.: The Wegener-Bergeron-Findeisen Process – Its Discovery and Vital Importance for Weather and Climate, Meteorol. Z., 24, 455–461, https://doi.org/10.1127/metz/2015/0626, 2015.

Storer, R. L., van den Heever, S. C., and Stephens, G. L.: Modeling Aerosol Impacts on Convective Storms in Different Environments, J. Atmos. Sci., 67, 3904–3915, https://doi.org/10.1175/2010JAS3363.1, 2010.

Sullivan, S. C., Lee, D., Oreopoulos, L., and Nenes, A.: Role of Updraft Velocity in Temporal Variability of Global Cloud Hydrometeor Number, P. Natl. Acad. Sci. USA, 113, 5791–5796, https://doi.org/10.1073/pnas.1514039113, 2016.

Tao, W.-K., Chen, J.-P., Li, Z., Wang, C., and Zhang, C.: Impact of Aerosols on Convective Clouds and Precipitation, Rev. Geophys., 50, RG2001, https://doi.org/10.1029/2011RG000369, 2012.

Terwey, W. D. and Rozoff, C. M.: Objective Convective Updraft Identification and Tracking: Part 1. Structure and Thermodynamics of Convection in the Rainband Regions of Two Hurricane Simulations, J. Geophys. Res.-Atmos., 119, 6470–6496, https://doi.org/10.1002/2013JD020904, 2014.

Thompson, G. and Eidhammer, T.: A Study of Aerosol Impacts on Clouds and Precipitation Development in a Large Winter Cyclone, J. Atmos. Sci., 71, 3636–3658, https://doi.org/10.1175/JAS-D-13-0305.1, 2014.

Thompson, G., Rasmussen, R. M., and Manning, K.: Explicit Forecasts of Winter Precipitation Using an Improved Bulk Microphysics Scheme. Part I: Description and Sensitivity Analysis, Mon. Weather Rev., 132, 519–542, https://doi.org/10.1175/1520-0493(2004)132<0519:EFOWPU>2.0.CO;2, 2004.

Thompson, G., Field, P. R., Rasmussen, R. M., and Hall, W. D.: Explicit Forecasts of Winter Precipitation Using an Improved Bulk Microphysics Scheme. Part II: Implementation of a New Snow Parameterization, Mon. Weather Rev., 136, 5095–5115, https://doi.org/10.1175/2008MWR2387.1, 2008.

van der Walt, S., Schönberger, J. L., Nunez-Iglesias, J., Boulogne, F., Warner, J. D., Yager, N., Gouillart, E., and Yu, T.: Scikit-Image: Image Processing in Python, PeerJ, 2, e453, https://doi.org/10.7717/peerj.453, 2014.

Varble, A.: Erroneous Attribution of Deep Convective Invigoration to Aerosol Concentration, J. Atmos. Sci., 75, 1351–1368, https://doi.org/10.1175/JAS-D-17-0217.1, 2018.

Wang, Y., Fan, J., Zhang, R., Leung, L. R., and Franklin, C.: Improving Bulk Microphysics Parameterizations in Simulations of Aerosol Effects, J. Geophys. Res.-Atmos., 118, 5361–5379, https://doi.org/10.1002/jgrd.50432, 2013.

Wegener, A.: Thermodynamik der Atmosphäre, J. A. Barth, Leipzig, oCLC: 39667532, 1911.

Weisman, M. L. and Klemp, J. B.: The Dependence of Numerically Simulated Convective Storms on Vertical Wind Shear and Buoyancy, Mon. Weather Rev., 110, 504–520, https://doi.org/10.1175/1520-0493(1982)110<0504:TDONSC>2.0.CO;2, 1982.

Weisman, M. L. and Klemp, J. B.: The Structure and Classification of Numerically Simulated Convective Storms in Directionally Varying Wind Shears, Mon. Weather Rev., 112, 2479–2498, https://doi.org/10.1175/1520-0493(1984)112<2479:TSACON>2.0.CO;2, 1984.

Weisman, M. L. and Rotunno, R.: The Use of Vertical Wind Shear versus Helicity in Interpreting Supercell Dynamics, J. Atmos. Sci., 57, 1452–1472, https://doi.org/10.1175/1520-0469(2000)057<1452:TUOVWS>2.0.CO;2, 2000.

White, B., Gryspeerdt, E., Stier, P., Morrison, H., Thompson, G., and Kipling, Z.: Uncertainty from the choice of microphysics scheme in convection-permitting models significantly exceeds aerosol effects, Atmos. Chem. Phys., 17, 12145–12175, https://doi.org/10.5194/acp-17-12145-2017, 2017.

WRF Community: Weather Research and Forecasting (WRF) Model, https://doi.org/10.5065/D6MK6B4K, 2000.

Zhang, K., Fu, R., Shaikh, M. J., Ghan, S., Wang, M., Leung, L. R., Dickinson, R. E., and Marengo, J.: Influence of Superparameterization and a Higher-Order Turbulence Closure on Rainfall Bias Over Amazonia in Community Atmosphere Model Version 5, J. Geophys. Res.-Atmos., 122, 9879–9902, https://doi.org/10.1002/2017JD026576, 2017.